Spectral boundary of the asymmetric simple exclusion process:
Free fermions, Bethe ansatz, and random matrix theory

Goran Nakerst [1,2] Tomaž Prosen [3] and Masudul Haque [1,2,4]

[1]*Institut für Theoretische Physik, Technische Universität Dresden, D-01062 Dresden, Germany*
[2]*Department of Theoretical Physics, Maynooth University, Co. Kildare, Ireland*
[3]*Department of Physics, Faculty for Mathematics and Physics, University of Ljubljana,*
Jadranska 19, SI-1000 Ljubljana, Ljubljana, Slovenia
[4]*Max-Planck-Institut für Physik Komplexer Systeme, D-01187 Dresden, Germany*

In nonequilibrium statistical mechanics, the asymmetric simple exclusion process (ASEP) serves as a paradigmatic example. We investigate the spectral characteristics of the ASEP, focusing on the spectral boundary of its generator matrix. We examine finite ASEP chains of length L, under periodic boundary conditions (PBCs) and open boundary conditions (OBCs). Notably, the spectral boundary exhibits L spikes for PBCs and $L + 1$ spikes for OBCs. Treating the ASEP generator as an interacting non-Hermitian fermionic model, we extend the model to have tunable interaction. In the noninteracting case, the analytically computed many-body spectrum shows a spectral boundary with prominent spikes. For PBCs, we use the coordinate Bethe ansatz to interpolate between the noninteracting case to the ASEP limit and show that these spikes stem from clustering of Bethe roots. The robustness of the spikes in the spectral boundary is demonstrated by linking the ASEP generator to random matrices with trace correlations or, equivalently, random graphs with distinct cycle structures, both displaying similar spiked spectral boundaries.

I. INTRODUCTION

The asymmetric simple exclusion process (ASEP) [1–11] is a well-studied paradigmatic stochastic many-body model that has been used to understand a wide range of nonequilibrium phenomena. This paper explores the spectral boundary of the Markov matrix (the generator of ASEP), with a focus on a characteristic spiky formation, by establishing connections between the ASEP, non-interacting fermions, and random matrices featuring trace correlations.

The ASEP model has proven instrumental in shedding light on phenomena like nonequilibrium phase transitions [5,12–16] and shock formation [16–21], among others. Its versatility extends across various domains, such as protein synthesis [22–24], intracellular transport [24–26], traffic flows [27], and quantum dots [28]. Another major incentive for its study is the association of the ASEP with interface dynamics and its connection to the Kardar-Parisi-Zhang equation in 1D (or equivalent noisy Burgers' equation) [29–32].

The ASEP is a model where particles move stochastically on a one-dimensional lattice, adhering to exclusion interactions that restrict each site to a single particle, mirroring volume exclusion in real systems. Particles move to adjacent sites only if these sites are unoccupied. The process is termed asymmetric due to the unequal probabilities for particle movement to the left or right, leading to directional bias. In cases where movement is limited to one direction, the model is referred to as totally asymmetric simple exclusion process (TASEP).

A probability vector P of particle configurations evolves according to the equation

$$\frac{d}{dt}P(t) = HP(t), \tag{1}$$

where H is the generator matrix that governs the dynamics of the system. This Markov (stochastic) matrix is a cornerstone of our study as it encapsulates all the dynamical information of the ASEP. The spectrum of H is particularly insightful: it informs us about the various rates at which different states of the system evolve, which is crucial for understanding how the system approaches its steady state.

The asymmetry of the ASEP implies that the matrix H is non-Hermitian and its eigenvalues are generally complex. The real part of these eigenvalues relates to the relaxation times of eigenmodes, indicating how quickly the system returns to the steady state after a disturbance. The imaginary part, on the other hand, determines the oscillatory behavior of the system, setting the timescales of periodic or quasiperiodic patterns in the system evolution.

In this paper, we focus on finite chains of length L and either periodic boundary conditions (PBCs) or open boundary conditions (OBCs). The finite-dimensional nature of H in these cases leads to a discrete and bounded spectrum. Analyzing this spectrum, especially establishing tight bounds on it, provides valuable insights into the aforementioned time scales and the overall dynamical properties of the system.

Our primary objective is to investigate and explain an intriguing feature of the shape of the spectral boundary, namely,
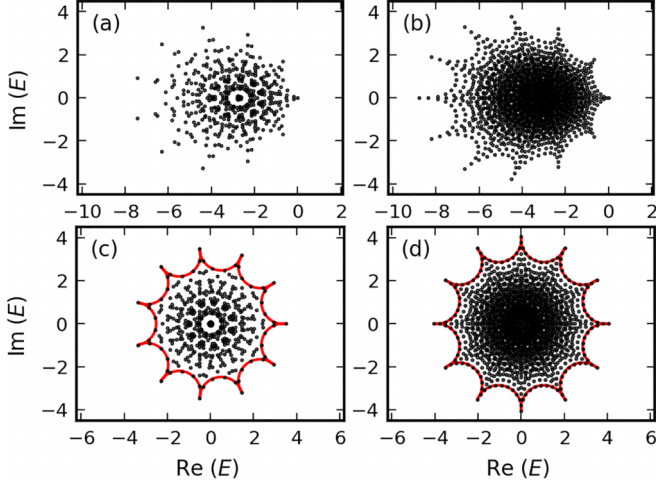
FIG. 1. Spectrum of the generator matrix H of TASEP (a), (b) and the noninteracting TASEP (c), (d) on $L = 11$ sites. The spectrum shows L spikes in (a), (c) for PBCs with $N = 5$ particles and $L + 1$ spikes in (b), (d) for OBCs. Red (gray in print) solid lines in (c), (d) denote the spectral boundary according to Eq. (24).

the prominent spikes clearly seen in Figs. 1(a) and 1(b) and also in previous studies [33,34]. The formation of these spikes (L spikes for PBCs and $L + 1$ for OBCs) present a fascinating aspect of the spectral characteristics of the ASEP. Unraveling the mechanisms behind the formation of these spikes in the spectral boundary is a major focus of this paper. We elucidate the emergence of spectral spikes through three approaches.

First, the generator matrix H is modeled as an interacting, non-Hermitian, spinless fermion system with interaction strength $U = 1$. For $U = 0$, H reduces to a noninteracting fermion model. Although this is not a Markov matrix, it is instructive to study the $U = 0$ case, as it is solvable as a non-Hermitian free-fermion Hamiltonian. (We refer to this as the noninteracting ASEP.) The many-body spectrum of H in this case, expressible as sums of single-particle eigenvalues on ellipses (circles for TASEP) in the complex plane, exhibits L spikes ($L + 1$ for OBCs) at its spectral boundary.

In the second approach, we use an extension of the coordinate Bethe ansatz method, traditionally used for calculating the spectrum of $U = 1$ with PBCs [32], which encompasses arbitrary interaction strengths U. For TASEP, the many-body spectrum is constituted by sums of Bethe roots, which exhibit an elliptical clustering in the complex plane within the range $0 \leqslant U \leqslant 1$. By focusing on the cluster sizes and disregarding finer Bethe root details, we demonstrate that the spectral boundary, akin to the $U = 0$ case, is defined by sums of Bethe roots from neighboring clusters, resulting in a prominent display of L spikes.

Lastly, we underscore the resilience of these spiky spectral boundaries by relating the TASEP to a random graph ensemble. In TASEP, the number of updates required to revert to a specific configuration is a multiple of L ($L + 1$ for OBCs) [33]. We examine random graphs wherein all cycle lengths are divisible by L ($L + 1$ for OBCs). Our findings reveal that the spectral boundaries of both the adjacency matrix (analogous to $U = 0$ in TASEP) and the Laplacian matrices (correspond-

ing to $U = 1$ in TASEP) of this random graph ensemble are characterized by the presence of L ($L + 1$) spikes.

The resilience of the spiky spectral boundary is noteworthy. This feature, inherent in the noninteracting fermion model, remarkably withstands the reintroduction of interactions. Furthermore, it prevails even when all aspects of H are disregarded, except for the cycle lengths in the many-body graph.

The paper is organized as follows: In Sec. II, we introduce the generator matrix of ASEP with PBCs and OBCs. In Secs. III and IV, we present results of the noninteracting ASEP ($U = 0$) with PBCs and OBCs, respectively. In Sec. V, we investigate the interacting TASEP ($0 \leqslant U \leqslant 1$) with PBCs by Bethe ansatz. In Sec. VI, we compare TASEP to random graphs with the aforementioned cycle structure. We conclude in Sec. VII. Appendixes A and B provide additional information on solving the noninteracting TASEP with OBCs. Appendix C details the derivation of Bethe equations for any U with PBCs and Appendix D presents numerical specifics for solving these equations to determine the full spectrum of the generator matrix H.

II. GENERATOR MATRIX OF ASEP

In this section, we will introduce the generator matrix H of the ASEP for PBCs and OBCs as non-Hermitian fermion models, along with essential notation.

We consider ASEP chains of length L. The number of particles in the chain is denoted by N and the particle density by $\rho = N/L$. The probability for a particle to hop right or left in time dt is $p \, dt$ or $q \, dt$, respectively, with the convention $p + q = 1$ unless specified otherwise.

Let us introduce

$$H = H_U = H_0 + U\mathcal{I}, \qquad (2)$$

where H_0 is a matrix with non-negative off-diagonal elements and zero diagonal entries and $\mathcal{I}$ is a diagonal matrix. The term U denotes the interaction strength. In the ASEP context, H_0 represents a noninteracting spinless fermion model, and $\mathcal{I}$ is a four-point (two-body) fermion interaction.

The generator of the ASEP is $H = H_1$ with interaction strength $U = 1$. Here, H_1 is the generator of a stochastic Markov process and a stochastic matrix, where the sums of all columns of H_1 equal zero. This property is ensured by the diagonal elements of $\mathcal{I}$ equaling the sums of the corresponding columns of H_0:

$$\mathcal{I}_{jj} = \sum_k (H_0)_{kj}. \qquad (3)$$

Whenever $U \neq 1$, H_U ceases to be a Markov matrix and does not generate the ASEP or any other stochastic process.

Studying H_U with $U \neq 1$ could elucidate the $U = 1$ case for two reasons. First, the analyticity of H_U in U suggests that its properties at $U \neq 1$ could be extrapolated to $U = 1$. Second, the diagonal matrix $\mathcal{I}$ exists only to ensure the Markov property of H_1 and, according to Eq. (3), is entirely determined by H_0. Therefore, ignoring $\mathcal{I}$ in the $U = 0$ case likely retains some features of the Markov matrix H_1.

A. Periodic boundary conditions

For PBCs, the matrices H_0 and $\mathcal{I}$ are given by

$$H_0 = \sum_{j=1}^{L} (p\sigma_{j+1}^+ \sigma_j^- + q\sigma_j^+ \sigma_{j+1}^-), \tag{4}$$

$$\mathcal{I} = \frac{1}{4} \sum_{j=1}^{L} (\sigma_j^z \sigma_{j+1}^z - 1). \tag{5}$$

The symbols $\sigma^\pm$ denote spin-raising and -lowering operators, while σ^z denotes the z-component of the spin. The spin-up state is interpreted as a particle present, while the spin-down state is interpreted as a particle absent.

Without loss of generality, we can assume $q \leqslant p$. For $p, q \neq 0$, the matrix H can be mapped to an XXZ spin-1/2 chain with non-Hermitian, twisted boundary conditions [9]. For $p = q$, the matrix H is Hermitian and for $U = 1$ reduces to the Heisenberg spin chain.

The matrix H can be written in terms of fermions by a Jordan-Wigner transformation

$$c_j^{(\dagger)} = e^{i\pi \sum_{k<j} \sigma_k^+ \sigma_k^-} \sigma_j^{-(+)}, \tag{6}$$

where $c_j^{(\dagger)}$ are fermionic annihiliation (creation) operators. The corresponding fermionic operator H is then given by

$$H_0 = \sum_{j=1}^{L-1} (p c_{j+1}^\dagger c_j + q c_j^\dagger c_{j+1}) + (-1)^{N+1} (p c_1^\dagger c_L + q c_L^\dagger c_1), \tag{7}$$

$$\mathcal{I} = \sum_{j=1}^{L} c_j^\dagger c_j c_{j+1}^\dagger c_{j+1} - N. \tag{8}$$

H_0 is the Hamiltoninian of non-Hermitian free spinless fermions, while $\mathcal{I}$ denotes a fermionic quartic interaction. The off-diagonal elements of H given by H_0 are non-negative, while the diagonal of the diagonal matrix $\mathcal{I}$ consists of non-positive values.

The number of particles N (spin-up states) is conserved by H for all interaction strengths U. The spectrum of H is invariant under exchanging p with q, since this change corresponds to taking the transpose of H.

B. Open boundary conditions

For OBCs, the matrix H_0 is given by

$$H_0 = \sum_{j=1}^{L-1} (p\sigma_{j+1}^+ \sigma_j^- + q\sigma_j^+ \sigma_{j+1}^-) + \alpha\sigma_1^+ + \gamma\sigma_1^- + \beta\sigma_L^- + \delta\sigma_L^+, \tag{9}$$

while the diagonal $\mathcal{I}$ is given by

$$\mathcal{I} = \frac{1}{4} \sum_{j=1}^{L-1} (\sigma_j^z \sigma_{j+1}^z - 1)$$
$$+ \frac{1}{2}\left[\left(\frac{p-q}{2} - \alpha + \gamma\right)\sigma_1^z + \left(\frac{q-p}{2} - \delta + \beta\right)\sigma_L^z\right]$$
$$- \frac{1}{2}[\alpha + \beta + \gamma + \delta]. \tag{10}$$

The bulk term of H_0 for OBCs is the same as for PBCs. The terms at the edges of the chain on site 1 and L with parameters $\alpha, \beta, \gamma, \delta$ denote particles hopping in and out of the chain from an infinite reservoir of particles. Similar to PBCs and $p, q \neq 0$, H can be mapped to an XXZ chain with non-Hermitian, twisted boundary conditions [35].

As in the PBC case, the operator H can be written in terms of fermions. The single spin operators at the end of the chain on site 1 and L hinder a straightforward application of a Jordan-Wigner transformation. Instead, we treat the infinite reservoir as an additional site. We enlarge the chain of length L to a ring of length $L+1$ and change the terms connecting to site $L+1$ accordingly. This is formally done by application of the well-known Kramers-Wannier duality transformation [36] $\sigma_j^x \rightarrow \prod_{l=1}^{j} \sigma_l^z$ and $\sigma_j^z \rightarrow \sigma_j^x \sigma_{j+1}^x$. The details are in Appendix A. Adding a site to the chain comes with the caveat that the multiplicity of every eigenvalue of the so-transformed H_0 is doubled.

To keep the algebra simpler, we restrict to the TASEP case $p = 1$ and $q = \gamma = \delta = 0$, leaving α and β as free parameters. The following results can be straightforwardly generalized to arbitrary p, q, γ, δ. As outlined in Appendix A, the Hamiltonian H_0 is expressible in terms of spinless fermions $c, c^\dagger$ as

$$H_0 = \alpha(c_{L+1} - c_{L+1}^\dagger)c_1^\dagger + \sum_{j=1}^{L-1} [c_j c_{j+1}^\dagger]$$
$$+ (-1)^L \mathcal{P}_c \beta c_L (c_{L+1} + c_{L+1}^\dagger), \tag{11}$$

where $\mathcal{P}_c$ denotes the parity of the fermion number

$$\mathcal{P}_c = (-1)^{\sum_{j=1}^{L+1} c_j^\dagger c_j} = (-1)^N, \tag{12}$$

which is conserved by H_0. Restricted to a fixed parity sector, H_0 is a quadratic Hamiltonian. The corresponding spectrum is the same for each parity sector, leading to the aforementioned doubling of the spectral multiplicity. This will be shown in detail in Sec. IV B.

In summary, the noninteracting TASEP H_0 on L sites with OBCs can be written as a free fermion model on $L+1$ sites, with twisted PBCs and superconducting terms $c_{L,1}^{(\dagger)} c_{L+1}^{(\dagger)}$ connecting to the additional site $L+1$.

C. Spectrum

All eigenvalues of H are either real or come in complex conjugate pairs. This characteristic stems from the fact that H can be represented as a real matrix. Specifically, for the case where $U = 1$, the stochastic nature of H dictates that its spectrum is situated in the left half of the complex plane.

Figure 1 presents the spectrum of TASEP on a lattice with $L = 11$ sites. The spectral boundary shows L spikes for PBCs ($N = 5$ particles) for $U = 1$ in (a) and $U = 0$ in (c) and $L + 1$ spikes for OBCs and $U = 1$ in (b) and $U = 0$ in (d). For OBCs, the parameters corresponding to the reservoirs are chosen as $\alpha = \beta = 1$ and $\gamma = \delta = 0$. The subsequent sections primarily aim to derive the mechanism responsible for the spikes in the spectral boundary.

Figures 1(c) and 1(d) reveal a highly structured spectrum for the noninteracting TASEP H_0, exhibiting rotational invariance at angles $2\pi/L$ for PBCs and $2\pi/(L+1)$ for OBCs. This
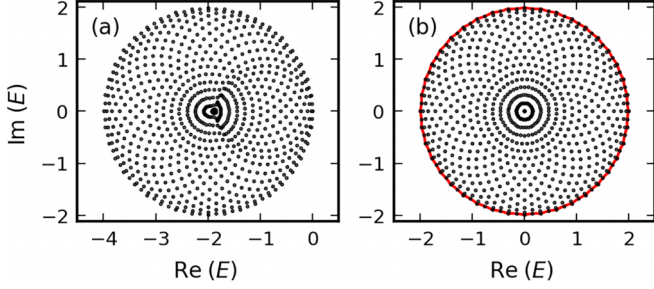
FIG. 2. Spectrum of the generator matrix H of TASEP (a) and the noninteracting TASEP (b) on $L = 40$ sites with $N = 2$ particles (dilute limit). The red (gray in print) solid line in (b) denotes the spectral boundary according to Eq. (24). The spectral boundary appears smooth and nonspiky in both panels.

characteristic stems from a quasisymmetry of H_0, which is investigated in detail in Secs. III and IV.

For TASEP with OBCs, the spectral boundary spikes are always prominent, as illustrated for the noninteracting TASEP in Sec. IV. However, this is not the case for PBCs. In Fig. 2(a), the spectrum of the PBC TASEP ($U = 1$) and in (b) its noninteracting variant ($U = 0$) are presented for $L = 40$ sites and $N = 2$ particles, without any noticeable spikes in the spectral boundary. Section III will demonstrate that, technically, the spectral boundary of the noninteracting TASEP has $L = 40$ spikes, but their distinctiveness fades in the dilute limit where $\rho \to 0$.

III. NONINTERACTING ASEP WITH PBC

In this section, we investigate the spectrum of the noninteracting ASEP H_0 for PBCs given by Eqs. (4) and (7), respectively. Section III A is devoted to the calculation of the single-body eigenvalues of H_0. In Sec. III B, we show the rotational invariance of the many-body spectrum of TASEP and in Sec. III C we combine the results from the preceding subsections and show how the spiky spectral boundary emerges. We quantify the prominence of the spikes in Sec. III D and comment on whether they survive in the limit of large L.

A. Single-body spectrum

Let us focus on the totally asymmetric case $p = 1$ and $q = 0$ first. Considering the single-body sector of H_0 as given in Eq. (7), we see that the single-body spectrum λ is given by roots of the polynomial:

$$\lambda^L + (-1)^{N+1}. \tag{13}$$

The roots are given by $\lambda = \omega^j$, where $\omega = e^{i\pi/L}$ and $0 \leqslant j < 2L$ runs over all even (odd) integers when N is odd (even). Thus, the single-body spectrum lies on the unit circle. In Fig. 3(a), the single-body spectrum for $p = 1$ and $q = 0$ and $L = 11$ and odd N is shown together with the unit circle.

For arbitrary values of p and q, the single-body spectrum is represented as
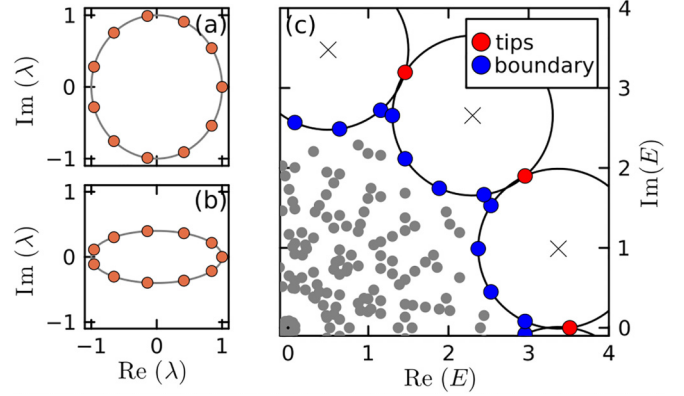
$$\lambda = p\omega^j + q\omega^{-j}, \tag{14}$$

FIG. 3. Spectrum of the noninteracting TASEP H_0 on $L = 11$ sites with PBCs. Single-body eigenvalues with $p = 1$ and $q = 0$ in (a) and $p = 0.7$ and $q = 0.3$ in (b). In (c), (part of) many-body spectrum with $N = 5$ particles highlighting the tips of the spikes (red, gray in print) and other boundary eigenvalues (blue, black in print). All boundary eigenvalues are located on circles of radius 1, with crosses marking the midpoints.

with j defined as previously. This spectrum lies on an ellipse with foci at $\pm 2\sqrt{pq}$ and semimajor axis $p + q$ and semiminor axis $p - q$:

$$\{(p + q)\cos(t) + i(p - q)\sin(t) : 0 \leqslant t \leqslant 2\pi\}. \tag{15}$$

Figure 3(b) illustrates the single-body spectrum for $p = 0.7$ and $q = 0.3$, alongside the ellipse defined by Eq. (15).

The structure of the single-body spectrum for any p, q suggests a straightforward relation with the totally asymmetric scenario $q = 0$. By modifying the imaginary component while maintaining the real part constant,

$$z \to \text{Re}\, z + i\frac{p + q}{p - q}\,\text{Im}\, z, \tag{16}$$

we can convert the single-body eigenvalues for general p, q values to those corresponding to the $q = 0$ case. This transforms the ellipse into a circle of radius $p + q$. Without loss of generality, we restrict ourselves to $p = 1$ and $q = 0$ for the remainder of this section.

B. Rotational invariance

With $p = 1$ and $q = 0$, the single-body spectrum remains unchanged under complex plane rotations of $2\pi/L$. This rotational invariance also applies to the many-body spectrum, which comprises sums of single-body eigenvalues.

Furthermore, this symmetry is evident in H_0 when transforming spin and fermionic operators. Transforming $c_j \to e^{-i2\pi j/L}c_j = \tilde{c}_j$ and $c_j^\dagger \to e^{i2\pi j/L}c_j^\dagger = \tilde{c}_j^\dagger$, or in terms of spin operators $\sigma_j^\pm \to e^{\pm i2\pi j/L}\sigma_j^\pm = \tilde{\sigma}_j^\pm$, results in $e^{i2\pi/L}H_0 = \tilde{H}_0$. Here, $\tilde{H}_0$ is constructed like H_0, but using the modified operators $\tilde{c}, \tilde{c}^\dagger$ ($\tilde{\sigma}^\pm$). Since these altered operators maintain their respective (anti)commutation relations, the spectra of H_0 and $\tilde{H}_0$ are identical. Therefore, the spectrum of H_0 is invariant under $2\pi/L$ rotations.

C. Spectral boundary

The structure of the many-body spectrum as observed in Fig. 1 is now a consequence of the relation of single-body to many-body eigenvalues and the rotational symmetry.

For ease of notation, we define $\lambda_j = \omega^{2j}$ when N is odd, and $\lambda_j = \omega^{2j+1}$ for even N. The many-body eigenvalues are obtained by adding N of these L single-body eigenvalues. More precisely, the many-body eigenvalues E correspond uniquely to configurations $s = (s_1, \ldots, s_L) \in \{0, 1\}^L$, where $\sum_j s_j = N$, and are given by

$$E = \sum_{j=1}^{L} s_j \lambda_j. \tag{17}$$

The many-body eigenvalues E_t which appear at the spike tips have the highest absolute values and are derived from configurations s with contiguous nonzero s_j entries. Specifically, each of the L tips $E_t(j_0)$ is linked to an index $1 \leqslant j_0 \leqslant L$ and a configuration $s = s_t(j_0)$ with

$$s_j = \begin{cases} 1 & j_0 \leqslant j \leqslant j_0 + N - 1 \\ 0 & \text{otherwise.} \end{cases} \tag{18}$$

Here, $j \equiv j - L$ is applied for $j > L$. The eigenvalues $E_t(j_0)$ are calculated as

$$E_t(j_0) = \sum_{j=j_0}^{j_0+N-1} \lambda_j. \tag{19}$$

Configurations s that lead to spike tips are termed domain-wall configurations. The many-body eigenvalues E_t are depicted as red circles (light colored in print) in Fig. 3(c).

Boundary eigenvalues in the many-body spectrum arise from interpolating between configurations of adjacent spike tips. In these configurations, the domain walls differ by a shift of one site. The interpolation process between these two domain walls involves moving a single particle (or executing a single spin flip). As a result, the configurations formed contain a maximum of two domain walls, each separated by one site. Specifically, boundary configurations $s = s_b(j_0, l_0)$ are associated with indices $1 \leqslant j_0 \leqslant L$ and $j_0 \leqslant l_0 \leqslant j_0 + N$, defined as

$$s_j = \begin{cases} 1 & j_0 \leqslant j \leqslant j_0 + N \text{ and } j \neq l_0 \\ 0 & j = l_0 \\ 0 & \text{otherwise.} \end{cases} \tag{20}$$

Again, $j \equiv j - L$ is used for $j > L$. The corresponding boundary eigenvalues $E_b(j_0, l_0)$ are computed by

$$E_b(j_0, l) = \sum_{j=j_0; j \neq l}^{j_0+N} \lambda_j. \tag{21}$$

When $l_0 = j_0$ or $l_0 = j_0 + N$ (indicating a single domain wall), the boundary eigenvalue matches a spike tip, $E_b(j_0, j_0) = E_t(j_0 + 1)$ or $E_b(j_0, j_0 + N) = E_t(j_0)$, respectively. The boundary eigenvalues $E_b(j_0, l)$ for $j_0 < l < j_0 + N$ are those many-body eigenvalues located between the spike tips $E_t(j_0)$ and $E_t(j_0 + 1)$, depicted as blue circles in Fig. 3(c).

Equation (21) can be reformulated as

$$E_b(j_0, l) = \sum_{j=j_0}^{j_0+N} \lambda_j - \lambda_l. \tag{22}$$

Given $|\lambda_l| = 1$ and the independence of the sum from l, all boundary eigenvalues are on L circles of radius 1. For $N \leqslant L/2$, the circle midpoints are the many-body spectrum tips $E_t^{(N+1)}(j_0)$ with $N + 1$ particles. The tips $E_t^{(N)}$ intersect two adjacent circles. This is illustrated in Fig. 3(c) with circles as black lines and midpoints as gray crosses.

According to Eq. (19), all tips reside on a circle with radius R, defined as

$$R = \left| \frac{1 - e^{i2\pi N/L}}{1 - e^{i2\pi/L}} \right| = \frac{\sin(\pi N/L)}{\sin(\pi/L)}. \tag{23}$$

This radius, combined with the circular pattern of the boundary eigenvalues, enables us to establish a continuous boundary for the many-body spectrum. It is formed by the intersection of all circles of radius 1 with the disk of radius R from Eq. (23). The boundary is parameterized by

$$z_B(t) = e^{-if(t)}(\gamma_1 + \gamma_2 e^{ig(kt)}), \tag{24}$$

with $\gamma_1 = \frac{\sin(\pi\rho)}{\sin(\pi/L)}$ and $\gamma_2 = 1$, with piecewise constant f,

$$f(t) = \frac{\pi}{L}\left(2\left\lfloor \frac{Lt}{2\pi} \right\rfloor - 1\right), \tag{25}$$

and g is piecewise the identity:

$$g(t) = \pi(1 - \rho) + \rho(t \bmod 2\pi). \tag{26}$$

The continuous boundary $z_B(t)$ is illustrated as a red (gray in print) curve in Fig. 1(c) for $L = 11$ and $N = 5$ and in Fig. 2(b) for $L = 40$ and $N = 2$. As expected, all boundary eigenvalues reside on the continuous boundary parametrized by $z_B(t)$.

Equation (24) is related to the spectral boundary of random matrices with higher-order cyclic correlations between L-tuples of matrix elements, akin to random graphs with a dominant cycle structure [37]. Their spectral boundary forms a hypotrochoidic curve, which is recovered from Eq. (24) by letting $f(t) = g(t) = t$. This relation hints at the connection between the spectral boundary of the noninteracting TASEP and random matrices; we explore this connection in Sec. VI.

A continuous spectral boundary has been derived for the TASEP ($U = 1$) as well [33]. It can be parametrized in terms of elementary functions and solutions of a differential equation.

D. Quantification of spikes

This subsection aims to measure the sharpness of the spectral boundary in the noninteracting TASEP, particularly focusing on whether spikes persist in large system sizes and, if so, how. For simplicity, we consider particle densities $0 \leqslant \rho \leqslant 1/2$. As the ASEP spectrum is invariant under changing $\rho \to 1 - \rho$, this comes with no loss of generality.

To assess the spikiness of the spectral boundary, we examine the ratio between two distances: d_t, the distance between spike tips, and d_b, the maximum extension of the spectral boundary beyond a circle of radius R. Recall, this circle of radius R represents the smallest enclosing disk for the TASEP

spectrum. d_b measures how far radius 1 circles, carrying the boundary eigenvalues, reach into the enclosing circle. A larger d_b relative to d_t indicates that these radius 1 circles extend more into the enclosing spectrum. Therefore, the ratio $2d_b/d_t$ quantifies the spikiness of the boundary. A value close to 1 suggests a spiky boundary, while a significantly smaller ratio implies a less spiky boundary. This factor of 2 arises because d_t pertains to the diameter of the boundary circles, whereas d_b is compared to their radius.

Following some simple trigonometry, one finds that the distances d_t and d_b are given by

$$d_t = 2\sin(\pi\rho) \tag{27}$$

and

$$d_b = 1 - \frac{\cos(\pi\rho + \pi/(2L))}{\cos(\pi/(2L))}. \tag{28}$$

The fraction $2d_b/d_t$ then simplifies to

$$\frac{2d_b}{d_t} = \tan(\pi\rho/2) + \tan(\pi/(2L)). \tag{29}$$

Equation (29) shows a monotonic increase with ρ, indicating that the spectral boundary becomes more pronouncedly spiky at higher ρ values. Due to the invariance of the spectrum under the transformation $\rho \to 1 - \rho$, the boundary reaches its maximum spikiness at $\rho = 1/2$.

The analytical findings are confirmed by panels (c) and (b) in Figs. 1 and 2, respectively. In Fig. 1(c), the many-body spectrum of H_0 is markedly spiky for $\rho = 5/11 \approx 0.45$, whereas in Fig. 2(b), the spectral boundary is nearly circular, aligning with the low ρ value of 2/40=0.05.

In examining the large L limit, we will explore two scenarios: the thermodynamic limit, where both N and L increase to infinity while maintaining a fixed ρ, and the few-particle (dilute) limit, where N remains constant and only L approaches infinity.

1. Thermodynamic limit

In the thermodynamic limit, the distance d_t remains constant, whereas d_b approaches $1 - \cos(\pi/\rho)$. Consequently, the ratio $2d_b/d_t$ tends towards $\tan(\pi\rho/2)$. This implies that for any nonzero ρ, the spiky structure of the spectral boundary is preserved in the thermodynamic limit, becoming more pronounced with increasing ρ.

Figure 1(c) presents the many-body spectrum of the noninteracting TASEP for $L = 11$ and $N = 5$, with Fig. 3(c) offering a closer view of the spectral boundary. Here, $\rho \approx 0.45$ and $2d_b/d_t \approx 1.01$ indicate pronounced spikes of the spectral boundary, as evident.

Regarding the length scales at which these spikes are observable, consider the following: The radius R of the spectrum scales as $O(L)$, necessitating a rescaling of the spectrum by $1/L$ to ensure a well-defined spectral density in the thermodynamic limit. At an infinite L, this rescaled spectrum densely fills the unit circle. For finite L, the tips of the spikes are spaced at a distance of $d_t = O(1/L)$ and the distance d_b of the spectral boundary from the unit circle is also $O(1/L)$.

Therefore, at the length scale of $1/L$, the spiky nature of the spectral boundary is distinctly visible.

2. Dilute limit (large L, constant N)

In the scenario where N is fixed and L increases, both distances d_t and d_b decrease, scaling as $O(1/L)$ and $O(1/L^2)$, respectively. Consequently, the ratio $2d_b/d_t$ tends towards 0, as indicated by Eq. (29). Therefore, in this limit, the spiky structure of the spectral boundary does not persist.

Figure 2 shows the many-body spectrum of the TASEP for $L = 40$ and $N = 2$, representative of the dilute limit. We show both a TASEP case ($U = 1$) and a noninteracting TASEP case ($U = 0$). With a $2d_b/d_t$ ratio of ≈ 0.01, it reveals a nonspiky spectral boundary, barely distinguishable from a circle, as shown by the red curve (gray in print) in Fig. 2(b).

IV. NONINTERACTING TASEP WITH OBC

In this section, we will present the analytical derivation of the many-body spectrum of the noninteracting TASEP H_0 with OBCs, specifically for $p = 1$ and $q = \gamma = \delta = 0$. Generalizations to arbitrary p, q, γ, δ are straightforward.

In Sec. IV A, we establish the rotational invariance of the spectrum of H_0. In Sec. IV B, we derive its single-particle spectrum and demonstrate its relation to the many-body eigenvalues. Section IV C demonstrates that the spectral boundary of H_0, similar to the PBC case, is defined by the intersection of circles with a disk, featuring $L + 1$ spikes. In the limit of large L, this boundary is akin to the PBC case with density $\rho = 1/2$, highlighted in Sec. IV D.

A. Rotational symmetry

The spectrum of the noninteracting TASEP H_0 is invariant under rotations of angle $\frac{2\pi}{L+1}$. Similar to the PBC case, consider the change of operators $c_j^\dagger \to e^{i\frac{2\pi}{L+1}j}c_j^\dagger = \tilde{c}_j^\dagger$ and $c_j \to e^{-i\frac{2\pi}{L+1}j}c_j = \tilde{c}_j$ or, equivalently, $\sigma_j^\pm \to e^{\pm i\frac{2\pi}{L+1}j}\sigma_j^\pm = \tilde{\sigma}^\pm$. This change implies that $e^{i\frac{2\pi}{L+1}}H_0 = \tilde{H}_0$, where $\tilde{H}_0$ is H_0 with c, $c^\dagger$ (σ) replaced by the tilde operators. As the tilde operators fulfill the canonical (anti)commutation relations of fermion operators (Pauli matrices), the spectrum of the noninteracting TASEP is invariant under rotations of angle $\frac{2\pi}{L+1}$.

B. Single- and many-body spectrum

Before we diagonalize H_0, let us specify the parity sector as $s = (-1)^L \mathcal{P}_c$. To simplify the following arguments, we will abuse notation and not distinguish between H_0 and H_0 restricted to a subspace of constant parity. At the end of this subsection, we will take the difference into account properly.

Let us collect the Dirac fermion operators c, $c^\dagger$ into a ($2L + 2$)-dimensional vector $\boldsymbol{c} = (c_1, \ldots, c_{L+1}, c_1^\dagger, \ldots, c_{L+1}^\dagger)^t$. We express H_0 given by Eq. (11) as

$$H_0 = \frac{1}{2}\boldsymbol{c}^\dagger \begin{pmatrix} A & B \\ C & -A^t \end{pmatrix} \boldsymbol{c} = \frac{1}{2}\boldsymbol{c}^\dagger M_c \boldsymbol{c}, \tag{30}$$

where the $(L+1) \times (L+1)$-matrices $A, B,$ and C are given by

$$A_{ij} = -\delta_{i,j+1\text{mod}(L+1)} + (1-\beta s)\delta_{i,L+1}\delta_{j,L}$$
$$+ (1-\alpha)\delta_{i,1}\delta_{j,L+1}, \tag{31}$$

$$B_{ij} = \alpha(\delta_{i,1}\delta_{j,L+1} - \delta_{i,L+1}\delta_{j,1}), \tag{32}$$

$$C_{ij} = \beta s(\delta_{i,L}\delta_{j,L+1} - \delta_{i,L+1}\delta_{j,L}), \tag{33}$$

and δ denotes the Kronecker-delta symbol.

The matrix A is, up to deformations in the $(1, L+1)$th and $(L+1, L)$th entries, a circulant matrix with only one nonzero off-diagonal. The matrices B and C only contain two nonzero entries. Thus, the solutions λ and u to the eigenvalue problem

$$M_c u = \lambda u \tag{34}$$

are closely related to the eigendecomposition of circulant matrices, which in turn are given by Fourier transforms. As shown in detail in Appendix B, the eigenvalues λ are solutions of

$$\lambda^{2L+2} = 4(\alpha\beta)^2(-1)^L \tag{35}$$

and are independent of the parity sector s. Since the polynomial in Eq. (35) is of even degree, its roots appear in pairs of $\pm\lambda$.

The Hamiltonian H_0 in Eq. (11) is non-Hermitian, preventing the direct use of the (Hermitian) Bogoliubov-de-Gennes formalism for linking the eigenvalues of M_c to the many-body spectrum of H_0. Hence, we will pursue an alternative method. We proceed as in Ref. [38] and express $c, c^\dagger$ in terms of Majorana fermions:

$$\phi_{j,1} = \frac{1}{\sqrt{2}}(c_j + c_j^\dagger), \quad \phi_{j,2} = \frac{1}{i\sqrt{2}}(c_j - c_j^\dagger). \tag{36}$$

After collecting the Majorana fermions $\phi_{j,l}$ into a column vector $\boldsymbol{\phi} = (\phi_{1,1}, \phi_{1,2}, \ldots, \phi_{L+1,1}, \phi_{L+1,2})^t$, H_0 can be written as

$$H_0 = \tfrac{1}{2}\boldsymbol{\phi}^t M_\phi \boldsymbol{\phi}, \tag{37}$$

where the matrix M_ϕ is a complex and antisymmetric $(2L+2) \times (2L+2)$ matrix. The transformation of Majorana fermions ϕ to Dirac fermions c via Eqs. (36) is unitary, making M_ϕ and M_c unitarily equivalent and hence sharing the same eigenvalues.

As M_ϕ is antisymmetric, it can be factorized [38] as

$$M_\phi = \tfrac{1}{2}V\Lambda J V^t, \tag{38}$$

where

$$V^t V = J = \text{Id}_{L+1} \otimes \begin{pmatrix} 0 & 1 \\ 1 & 0 \end{pmatrix}. \tag{39}$$

Id_{L+1} denotes the $(L+1) \times (L+1)$ identity matrix and Λ is a diagonal matrix containing the eigenvalues of M_ϕ (M_c). The antisymmetry of M_ϕ implies that its eigenvalues come in pairs $\pm\lambda$, which is consistent with the solutions of Eq. (35). The diagonal of Λ is ordered as $\lambda_1, -\lambda_1, \ldots \lambda_{L+1}, -\lambda_{L+1}$. We fix the choice between λ_j and $-\lambda_j$ by requiring $\text{Re}\,\lambda_j \geqslant 0$.

Let us define another type of Dirac fermions b, b' as

$$(b_1, b_1', \ldots, b_{L+1}, b_{L+1}')^t = (V^t\boldsymbol{\phi}). \tag{40}$$

These fulfill the usual anticommutation relations of Dirac fermions [38], but b' is, in general, not the Hermitian adjoint of b. Nevertheless, the Hamiltonian H_0 becomes diagonal in terms of b, b':

$$H_0 = \sum_{j=1}^{L+1} \lambda_j b_j' b_j - \frac{1}{2}\sum_{j=1}^{L+1} \lambda_j. \tag{41}$$

The eigenstates of H_0 are given by creation operators b_j' acting on the vacuum $|0\rangle_b$, which are 2^{L+1} in total. But not all eigenstates correspond to an eigenvalue of H_0 given by Eq. (11). We have to take into account that the Dirac fermions b, b' are only defined on fixed parity subspaces.

We numerically find that the parity operator $\mathcal{P}_b$ of the b, b' fermions obeys

$$\mathcal{P}_b = -s\mathcal{P}_c, \tag{42}$$

where P_c denotes the parity operator of the c fermions. Recall that we let $s = (-1)^L \mathcal{P}_c$ at the beginning of this subsection. Thus, the admissible b'-fermion states must have b-parity $\mathcal{P}_b = -(-1)^L = (-1)^{L+1}$. Especially, the parity of the admissible b-fermion states does not depend on s. Thus, both parity sectors give rise to the same many-body spectrum of H_0 in Eq. (41), as required.

In summary, the many-body spectrum of the noninteracting TASEP, subject to a global shift in the complex plane, is represented by the sums of the $L+1$ roots from Eq. (35) with positive real parts. These are scaled roots of ±1 with magnitude proportional to $(\alpha\beta)^{1/(L+1)}$. Depending on whether L is odd or even, an even or odd number of summands, respectively, are included in the sums.

C. Spectral boundary

The emergence of the many-body spectrum of the non-interacting TASEP with OBCs follows a similar principle than for PBCs discussed in Sec. III: the many-body spectrum consists of sums of (scaled) roots of ±1. In the following, we describe how the spiky spectral boundary emerges for OBCs. Especially, we will demonstrate that, akin to the PBC case, the spectral boundary resides on $L+1$ circles, each with a radius of $(2\alpha\beta)^{1/(L+1)}$, and provide a comparable parametrization for this boundary.

In the following, we focus exclusively on the spectral boundary associated with the most negative real parts. This is illustrated in Figs. 4(a) and 4(b), where the eigenvalues of the relevant sectors are marked with blue and red circles. The rotational symmetry of the spectrum means that the structure of the boundary is a repetitive pattern reflecting the shape of sectors with the smallest real parts. Hence, restriction to sectors with the most negative real part eigenvalues comes with no loss of generality.

Let us first consider even L. Recall that the many-body spectrum is given by sums of an odd number of positive real part roots of the polynomial in Eq. (35). Let us denote the $L+1$ roots with non-negative real part by $\lambda_1, \ldots, \lambda_{L+1}$. Then the $L+1$ many-body eigenvalues with the smallest real parts
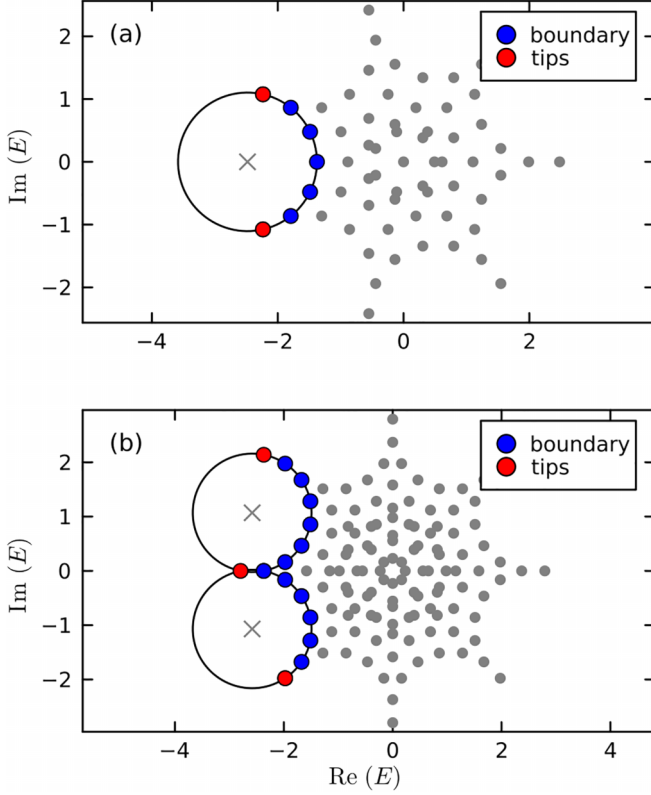
FIG. 4. Many-body spectrum of the noninteracting TASEP with OBCs on (a) $L = 6$ and (b) $L = 7$ sites. Similar to PBCs in Fig. 3(c), all boundary eigenvalues lie on circles, with midpoints denoted by crosses.

are eigenvalues lying on the spectral boundary and given by

$$\lambda_j - \frac{1}{2} \sum_{l=1}^{L+1} \lambda_l. \tag{43}$$

If we label λ_l by increasing angle with a branch cut on the negative imaginary axis, then the tips of the spectrum are given by the indices $j = 1$ and $j = L + 1$.

In Fig. 4(a), we show the spectrum of the noninteracting TASEP with OBCs on $L = 6$ sites. The spectrum shows $L + 1 = 7$ spikes. The boundary and tips according to Eq. (43) are shown as blue and red markers, respectively. The markers lie on a circle with midpoint $-\frac{1}{2} \sum_{l=1}^{L+1} \lambda_l$ and radius $|\lambda_j| = (2\alpha\beta)^{1/(L+1)}$.

Let us now consider the slightly more complicated case of odd L. In Fig. 4(b), we show the many-body spectrum on $L = 7$ sites. The tip of the spectral edge with the smallest real part is given by an empty sum of λ_l's and thus is $-\frac{1}{2} \sum_{l=1}^{L+1} \lambda_l$. The boundary eigenvalues are given by the following (shifted) sum of two single-particle eigenvalues:

$$\lambda_j + \lambda_{1,L+1} - \frac{1}{2} \sum_{l=1}^{L+1} \lambda_l, \tag{44}$$

where $2 \leqslant j \leqslant L$ and λ_1 corresponds to the lower spectral boundary in Fig. 4(b) while λ_{L+1} corresponds to the upper part. The midpoints of the circles are given by $\lambda_{1,L+1} - \frac{1}{2} \sum_{l=1}^{L+1} \lambda_l$ and the radius again by $|\lambda_j| = (2\alpha\beta)^{1/(L+1)}$.

Similar to the PBC case, we can establish a continuous boundary for the many-body spectrum, parametrized by Eq. (24). In the OBC case, the constants $\gamma_{1,2}$ are given by

$$\gamma_1 = (2\alpha\beta)^{1/(L+1)} \frac{1}{2 \sin(\pi/(2L+2))}, \tag{45}$$

$$\gamma_2 = (2\alpha\beta)^{1/(L+1)}, \tag{46}$$

while the piecewise constant f and the piecewise identify function g are given by

$$f(t) = \frac{\pi}{L} \left(2 \left\lfloor \frac{Lt}{2\pi} \right\rfloor - 1 \right), \tag{47}$$

$$g(t) = \pi \frac{L+2}{2L+2} + \frac{L}{2L+2}(t \bmod 2\pi). \tag{48}$$

The continuous boundary $z_B(t)$ with the above parameters is illustrated in Fig. 1(d) as a red (gray in print) curve for $L = 11$.

D. Spikes in the large L limit

The parametrization of the spectral boundary for OBCs shows a clear link to the spectral boundary for PBCs. Specifically, in the large L limit with constant α, β, the OBC spectral boundary aligns with the PBC case at $\rho = 1/2$. This relation is immediately evident for γ_2, f, and g. Further, a series expansion of γ_1 for large L reveals that its leading term, $\gamma_1 = L/\pi + O(1)$, is identical in both cases, with differences emerging only at $O(1)$.

Consequently, in the large L limit, the spiky spectral boundary in the OBC case remains pronounced. Rescaling the spectrum by $1/L$, the spectral density approaches filling the unit disk as $L \to \infty$. For finite L, the tips are spaced by $O(1/L)$, and the maximum deviation of the boundary from the unit circle is also $O(1/L)$.

V. PBC TASEP BY BETHE ANSATZ

In Sec. III, we showed that in the noninteracting TASEP ($U = 0$) with PBCs, the spiky boundary of the many-body spectrum emerges essentially as sums of evenly spaced single-body eigenvalues $\lambda_1, \ldots, \lambda_L$. This section expands that concept to interaction strengths $0 < U$. Employing the coordinate Bethe ansatz, we generalize the single-body framework to Bethe roots, which tend to cluster close to $\lambda_1, \ldots, \lambda_L$. This clustering, combined with TASEP many-body eigenvalues being sums of Bethe roots, results in a spiky spectral boundary for any interaction strength $0 \leqslant U \leqslant 1$.

This section focuses on $\rho \approx 1/2$, where the most prominent spectral boundary spikes in the noninteracting ASEP were observed. In the low-density limit (ρ approaching zero), we anticipate a spectral boundary for the usual ASEP similar to the noninteracting case, characterized by a smooth, circular boundary without spikes. Figure 2 partly supports this, showing similar many-body spectra for TASEP with $U = 1$ (a) and $U = 0$ (b), both featuring smooth, nonspiky spectral boundaries.

In Sec. V A, we express the eigenvalues of H for arbitrary U in terms of the coordinate Bethe ansatz, with derivation details and numerical solution methods presented in Appendixes C and D. In Sec. V B, we demonstrate the clustering

of solutions to the Bethe equations and in Sec. V C, we establish how this clustering results in a spiky spectral boundary.

A. Coordinate Bethe ansatz

The coordinate Bethe ansatz has been used extensively for ASEP [6,9–11,32–34,39–60] and for various variants and extensions of ASEP [9,58,61–91]. The Bethe ansatz eigenvalues E for arbitrary U are given by

$$E = \sum_{j=1}^{N} \left(q z_j + p z_j^{-1} - U \right), \tag{49}$$

where z_j are complex numbers, the so-called Bethe roots, which in turn are solutions of the following recurrent relations:

$$z_j^L = \prod_{k=1;k\neq j}^{N} \left(-\frac{p + q z_j z_k - U z_j}{p + q z_j z_k - U z_k} \right). \tag{50}$$

The solutions of Eq. (50) are N-tuples $(z_1, \ldots, z_N)$ and each N-tuple gives rise to an eigenvalue E of the TASEP H via Eq. (49).

The Bethe equations for general U have been derived for TASEP in Ref. [41] and for ASEP in Ref. [92]; although presented differently from Eqs. (49) and (50). In Appendix C, we present a derivation of the Bethe equations in terms of U closely following [32].

Numerical data indicates that in small systems, each eigenvalue is a sum of Bethe roots, although a formal proof of the completeness of the Bethe ansatz is lacking [93–95]. In our finite ASEP system investigations, all eigenvalues conformed to the Bethe ansatz.

For $q = 1$ and $p = 0$, the eigenvalue equation simplifies to

$$E = \frac{1}{2} \sum_{j=1}^{N} (Z_j - U) \tag{51}$$

and the Bethe equations transform into

$$(U + Z_j)^{L-N} (U - Z_j)^N = -2^L \prod_{k=1}^{N} \frac{Z_k - U}{Z_k + U}, \tag{52}$$

with

$$Z_k = 2z_k - U \tag{53}$$

representing scaled, shifted Bethe roots. We refer to either the z_k or Z_k as the Bethe roots, depending on the context. In Eq. (52), the main simplification from the general p, q case is the independence of the right-hand side from j, which makes the solutions Z_j roots of the polynomial $P(Z) = (U + Z)^{L-N} (U - Z)^N - Y$, with Y given by the right-hand side of Eq. (52). This not only simplifies numerical computation of the Bethe roots Z_j, but also ensures their continuity in U [96]. Consequently, we will focus on the specific case of $q = 1$ and $p = 0$ for the rest of this section.

Appendix D details the numerical solution process for the Bethe Eqs. (52) and the systematic retrieval of all Bethe roots.

Equations (49) and (51) establish that many-body eigenvalues are sums of Bethe roots, up to a global shift. To
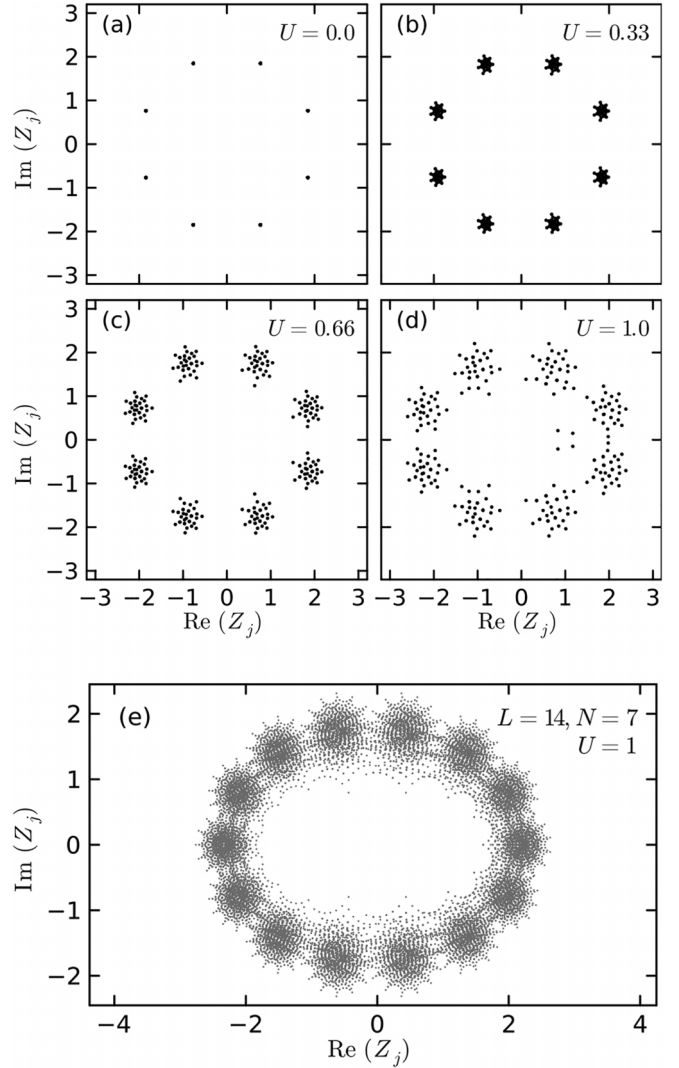

FIG. 5. All $N \times \binom{L}{N}$ Bethe roots Z_j of the TASEP. (a)–(d) $L = 8$, $N = 4$, for different values of U. (e) $L = 14$, $N = 7$, $U = 1$.

demonstrate a spiky spectral boundary, we will show numerically a sufficient clustering of Bethe roots, which is the focus of the rest of this section.

B. Clustering of the Bethe roots

To examine the spectral boundary in terms of the Bethe roots, we will consider in the complex plane the Bethe roots (z_j or Z_j) corresponding to each of the $\binom{L}{N}$ eigenstates. There are thus $N \times \binom{L}{N}$ Bethe roots in total, for any value of U. Such plots are shown in Fig. 5.

For $U = 0$, the Bethe roots z_j satisfy the equation $z_j^L = (Z_j/2)^L = (-1)^{N+1}$ and agree with the single-body eigenvalues of H_0 as stated in Eq. (14). Therefore, the many-body spectrum derived via the Bethe ansatz for $U = 0$ aligns with that of the noninteracting ASEP model discussed in Sec. III, as expected. An illustrative example of the Bethe roots $Z_j = 2z_j$ for $U = 0$ is provided in Fig. 5(a) for $L = 8$ and $N = 4$. Here, each solution of the Bethe equations contributes $N = 4$ roots, which together describe one of the $\binom{8}{4}$ eigenstates. We
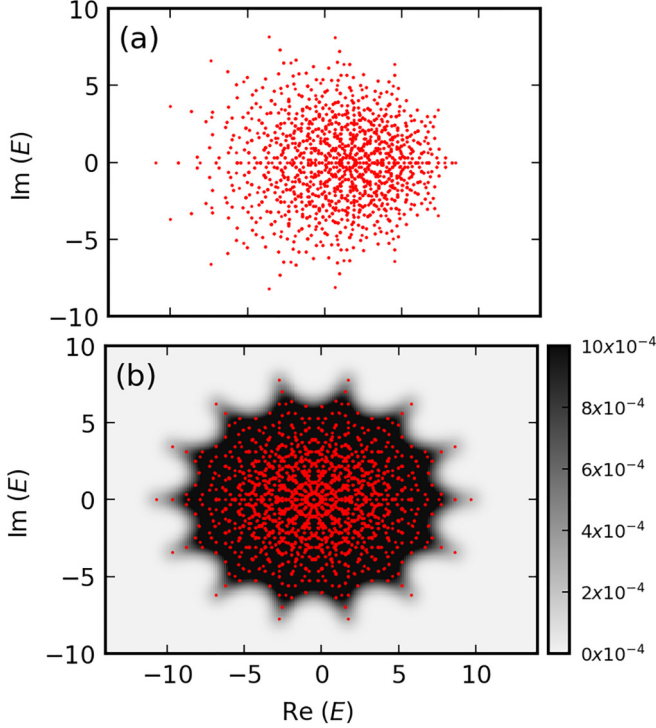
FIG. 6. (a) The many-body spectrum of TASEP with $L = 14$ and $N = 7$ (multiplied by 2 and shifted by N). (b) Probability density function of the many-body spectrum of the random Bethe roots Z for $L = 14$ and $N = 7$ capped at 10^{-3}. Red (gray in print) dots are the means of the complex Gaussians.

FIG. 7. The width σ of the complex Gaussians fitted to the clusters of the Bethe roots for $U = 1$ at half-filling $N = L/2$. The solid line denotes the average $\langle \sigma_j \rangle_j = \frac{1}{L} \sum_j \sigma_j$ of the cluster widths and the dotted line guides the eye to $L^{-1/2}$. The inset shows the absolute value of the centers of the complex Gaussians $|\mu|$. Black solid line indicates the average.

fit as $\mathcal{N}_j$, each characterized by its mean μ_j and standard deviation σ_j.

C. Structure of the many-body spectrum

In the following, we will show that by considering only the centers and widths of Bethe root clusters, and not their specific structure, we can approximate a many-body spectrum that mirrors key characteristics of the TASEP many-body spectrum, particularly its spiky boundary.

Recall that for $U = 0$, each many-body eigenvalue E is a sum of N out of L single-body eigenvalues. Specifically, E is given by

$$E = \sum_{j=1}^{L} s_j \lambda_j = \sum_{s_j \neq 0} \lambda_j, \qquad (54)$$

where $s \in \{0, 1\}^L$ is a configuration with $\sum_j s_j = N$ and λ_j are the single-particle eigenvalues determined in Sec. III C. By Eq. (51), every many-body eigenvalue of the TASEP ($U = 1$) corresponds to a sum of N Bethe roots $(Z_1, \dots, Z_N)$ and by the continuation from $U = 1$ to $U = 0$ each Bethe root Z_j belongs to one of the L clusters. Instead of summing solutions of the Bethe Eq. (52), we employ a statistical ansatz and consider random many-body eigenvalues of the form

$$E_{\text{rand}} = \sum_{j=1}^{L} s_j \mathcal{N}_j = \mathcal{N}_s, \qquad (55)$$

where $\mathcal{N}_s$ denotes a Gaussian with mean $\sum_{j=1}^{L} s_j \mu_j$ and variance $\sum_{j=1}^{L} s_j \sigma_j^2$. We refer to $\mathcal{N}_s$ as many-body Gaussians and denote their densities by f_s. The full random many-body spectrum is then given by

$$\frac{1}{\mathcal{Z}} \sum_{\substack{s \in \{0,1\}^L \\ s_1 + \dots + s_L = N}} f_s, \qquad (56)$$

plot all the $4 \times \binom{8}{4}$ roots together in a single plot. Since for $U = 0$ every solution to the Bethe equations is a subset of the 8 single-body eigenvalues of H_0, the union of all solutions is highly degenerate and only 8 unique markers show up in Fig. 5(a).

For $U > 0$, the degeneracy of the $U = 0$ case is lifted and the $4 \times \binom{8}{4}$ Bethe roots Z_j become distinct, as observed in Figs. 5(b)–5(d) for $U = 0.33$, 0.66, and $U = 1$, respectively. The continuity of Bethe roots z_j in U suggests that for small U, these roots should be proximate to the Lth roots of $(-1)^{N+1}$. Numerically, this is confirmed as the Bethe roots z_j tend to cluster around the Lth roots of $(-1)^{N+1}$ for small U. As depicted in Figs. 5(b) and 5(c) for $U = 0.33$ and $U = 0.66$, respectively, the Z_j's distinctly form $L = 8$ clusters around the Bethe roots for $U = 0$. This clustering is even discernible for $U = 1$, as shown in Fig. 5(d), where the $L = 8$ clusters remain identifiable.

For larger L, the Bethe root clusters overlap at $U = 1$, evident from Fig. 5(e) for $L = 14$ and $N = 7$. However, the statistical width of these clusters diminishes with larger L. This is demonstrated in Fig. 7, where the average cluster width decreases as $L^{-1/2}$ in the thermodynamic limit with $\rho = N/L = 1/2$ and $N, L \to \infty$.

We define the locations and widths of these clusters by fitting a Gaussian mixture model of L independent Gaussians $\mathcal{N}$ with complex means to the Bethe roots. The Bethe roots distribution is approximated as $\frac{1}{L} \sum_{j=1}^{L} f_j$, with f_j representing Gaussian densities. We label the Gaussians of the optimal
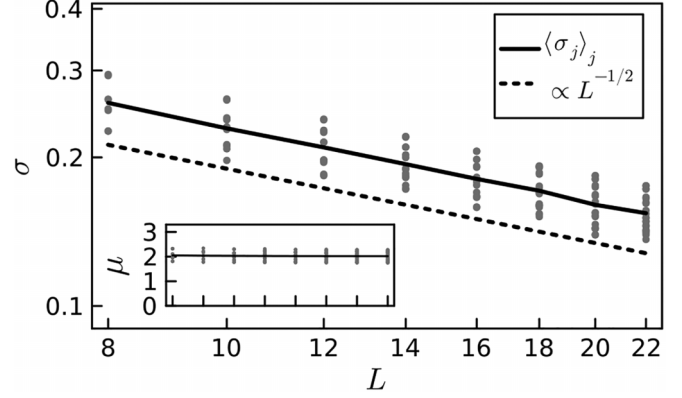
where $\mathcal{Z} = \binom{L}{N}$ is a normalization constant. Keep in mind that the Gaussians $\mathcal{N}_s$ for different configurations s are independent. The many-body spectrum of the TASEP is a specific sample of the distribution in Eq. (56). For $U = 0$, the random spectrum becomes deterministic and agrees with the noninteracting many-body spectrum presented in Sec. III.

In Fig. 6(b), we present the probability density from Eq. (56) for $L = 14$, $N = 7$, and $U = 1$, with the density capped at 10^{-3} for clarity. The red markers indicate the means $\sum_{j=1}^{L} s_j \mu_j$ of the many-body Gaussians $\mathcal{N}_s$. Both the discrete means and the continuous density exhibit pronounced spikes at the boundary. When these means are compared to the TASEP many-body spectrum shown in Fig. 6(a), even finer details of the spectrum are discernible in the structure of the means.

The boundary of the random many-body spectrum is mainly determined by Gaussians $\mathcal{N}_s$, associated with domain wall configurations of one or two domain walls, separated by at most one empty site, due to the exponential decay of the Gaussian probability density function. These configurations are identical to those defining the spectral boundary in the non-interacting case.

The random Bethe spectrum and the TASEP spectrum share a remarkably similar overall shape. However, differences do exist, e.g., the boundary of the random Bethe spectrum is not skewed leftward in the complex plane. This is attributed to the additional structure in the Bethe root clusters seen in Fig. 5, not represented by rotationally invariant Gaussians.

D. Thermodynamic limit

Similar to the noninteracting case with $U = 0$, we demonstrate that the spiky boundary persists in the thermodynamic limit as L and N increase while maintaining a fixed density $\rho = N/L$.

Let us first focus on the centers $\sum_{j=1}^{L} s_j \mu_j$ of the many-body Gaussians $\mathcal{N}_s$, depicted as red dots in Fig. 6. According to the inset of Fig. 7, the absolute values of $|\mu_j|$ appear to be independent of L. This independence suggests that the noninteracting case scenario also applies to the many-body Gaussian centers. For boundary configurations s, these centers, being sums of $N = \rho L$ nearby μ_j, scale with L. Given that both the tip distance (d_t from Sec. III D) and boundary depth (d_b from Sec. III D) are proportional to 1, the spiky structure of the boundary Gaussian centers is maintained in the thermodynamic limit.

However, this does not automatically mean that the spiky spectral boundary of the random spectrum, as defined in Eq. (56), persists in the thermodynamic limit. For this to hold true, the widths of the Gaussians $\mathcal{N}_j$ in the mixture model must decrease sufficiently fast.

Figure 7 displays the widths σ_j of $\mathcal{N}_j$ for the TASEP case ($U = 1$) at half-filling ($N = L/2$), with L ranging from 8 to 22. The cluster widths σ_j vary, being larger for clusters with smaller $|\operatorname{Re} Z|$ and smaller for those with larger $|\operatorname{Re} Z|$, as also observed in Fig. 5(e). Despite this variation, the widths σ_j are centered around their average $\langle \sigma_j \rangle_j = \frac{1}{L} \sum_{j=1}^{L} \sigma_j$, which decreases approximately as $\propto L^{-1/2}$, as shown by the dashed

line in Fig. 7. Consequently, the variance $\sigma_s = \sum_{j=1}^{L} s_j \sigma_j^2$ of the Gaussians $\mathcal{N}_s$ scales as $\propto 1$. This indicates that the standard deviation of the boundary Gaussians $\mathcal{N}_s$ remains on the order of $\propto 1$ even as L increases, aligning with the scale of both the tip distance and spike depths. Therefore, the spiky structure of the statistical many-body spectrum for $U = 1$ is preserved in the thermodynamic limit, as in the $U = 0$ case presented in Sec. III.

VI. THE RANDOM MATRIX PICTURE

In the previous sections, we showed that the spikes of the spectral boundary of the TASEP are a consequence of the many-body spectrum being generated by summing single-particle-like clusters.

This section demonstrates that the spiky spectral boundary is a prevalent characteristic in a broad range of systems, extending beyond free fermions or those solvable by the Bethe ansatz. Specifically, this feature is typical in systems where the many-body graph exhibits a particular cycle structure, with cycle lengths being integer multiples of the spike count.

A. From TASEP to graphs

The matrix elements of the generator of the noninteracting TASEP H_0 are either zero or one. Thus, the generator matrix is naturally interpreted as the adjacency matrix of a directed graph. This graph, which we will call the many-body graph of TASEP, has vertices representing particle configurations in the chain and edges indicating permissible transitions. For TASEP with $U = 1$, its generator matrix H is the negative combinatorial Laplacian of this graph.

B. Cycles of TASEP

The permissible transitions between particle configurations impose constraints on the structure of the many-body graph. Our focus is on the nature of cycles in the many-body graph, which are closed walks with only the start and end vertices being the same.

The cycle lengths in the TASEP many-body graph are divisible by L for PBCs and by $L + 1$ for OBCs [33]. This is evident in cycles among configurations, which only contain a single particle. These cycles consist of L particle movements ($L + 1$ for OBCs) such that the particle arrives at its original position.

The number of closed walks with length k is related to entries of the kth power of the adjacency matrix A ($A = H_0$ in the case of ASEP). The element $(A^k)_{ij}$ denotes the number of distinct walks of length k from vertex i to j. Thus, $(A^k)_{ii}$ counts the number of distinct closed walks with length k starting and ending at vertex i and $\operatorname{tr}(A^k)$ aggregates the total number of closed walks with length k. Especially, if $\operatorname{tr}(A^k) = 0$ then the graph does not contain any closed walks, thus any cycle, of length k.

In Fig. 8(e), we depict $\operatorname{tr}(A^k) + 1$ as blue squares, where $A = H_0$, plotted against $k = 1, \ldots, 2L$ for a system of $L = 12$ sites and PBCs with $N = 6$ particles. The addition of $+1$ facilitates a logarithmic scale on the y axis. Here, $\operatorname{tr}(A^k)$ equals zero for all values of k not divisible by L, indicating the
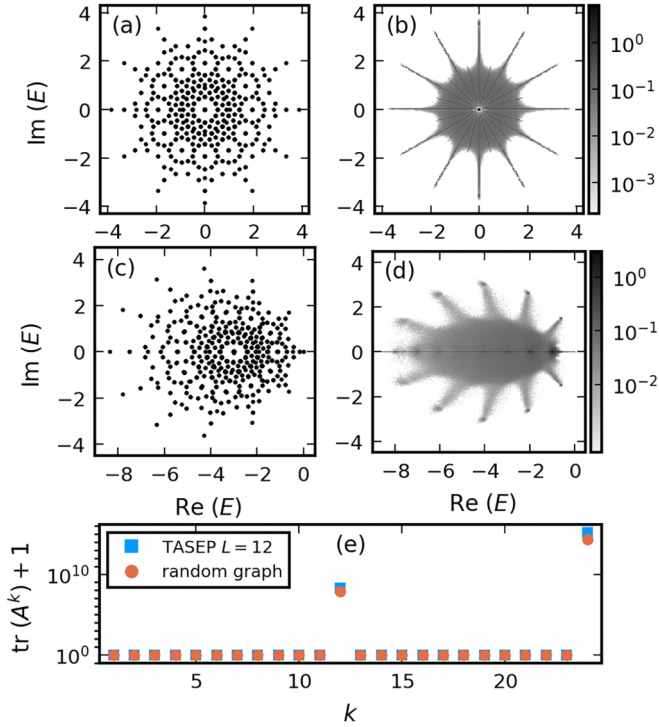
FIG. 8. TASEP spectrum (PBC) with $L = 12$ and $N = 6$ for (a) $U = 0$ and (c) $U = 1$. In (b) and (d), spectral density of random graphs with cycle length divisible by L; in (b) of the adjacency matrix and in (d) of the negative (combinatorial) Laplacian. In (e), traces of powers of the noninteracting TASEP H_0 (squares) and random graph adjacency matrix (circles).

absence of cycles in the graph with length $k \bmod L \neq 0$. Similarly, for OBCs, $\text{tr}(A)^k = 0$ if and only if $k \bmod L + 1 = 0$ (not shown).

C. Random graph model

To demonstrate the robustness of the spiky spectral boundary, we compare the TASEP spectrum with the spectral density of a random graph ensemble characterized only by cycles whose lengths are divisible by L. This comparison is focused on the TASEP with PBCs, noting that the OBC scenario can be similarly analyzed by simply adjusting L to $L + 1$.

We sample the random graph by initially forming a directed cycle with D vertices. Next, we randomly choose a vertex and traverse the graph randomly for $L - 1$ steps. The vertex reached after $L - 1$ steps is connected back to the starting vertex, creating a cycle of length L. This process is repeated until the graph contains a predetermined total number n of edges. When the number of vertices D is divisible by L, the construction of the graph ensures that all cycle lengths in the random graph are also divisible by L. We provide a mathematically rigorous argument in Appendix E.

Figure 8 contrasts the random graph ensemble to the TASEP with $L = 12$ sites and PBCs with $N = 6$ particles. Quantities of the random graph ensemble are averaged over 2000 samples, with the cycle length set to L and the number

of vertices $D = 924$, matching the Hilbert space dimension of the TASEP.

In Fig. 8(e), we present $\text{tr}(A^k) + 1$ for the random graph ensemble, shown as red circles. In this ensemble, $\text{tr}(A^k)$ is zero for all k that are not integer multiples of L. Whenever k is an integer multiple of L, $\text{tr}(A^k)$ for the adjacency matrix A of the random graph ensemble is comparable in magnitude to $\text{tr}(A^k)$ for $A = H_0$, the generator matrix of TASEP. This similarity suggests that the number of closed walks in the random graph ensemble is on par with that in the TASEP many-body graph.

Figures 8(a)–8(d) display a comparison between the random graph ensemble and TASEP, matching the parameters used in Fig. 8(e). In Figs. 8(a) and 8(b), we show the non-interacting TASEP spectrum alongside the estimated spectral density of the graph ensemble – both featuring L distinct spikes.

In Figs. 8(c) and 8(d), the focus is on the spectrum of TASEP ($U = 1$) and the spectral density of the negative graph Laplacian for the random graph ensemble. Notably, the random graph Laplacian also presents L pronounced spikes. The spike patterns, particularly their bending towards the left, show a resemblance to the TASEP spikes. The overall shape of the spectral density (ignoring the spikes) takes on a spindle-like form, characteristic of (sparse) random Markov matrices [97–100].

VII. CONCLUSION AND DISCUSSION

In this paper, we explored the connections among the spectral problems for ASEP, free fermion models, and random matrix theory, focusing particularly on the distinctive spiky shape of the ASEP spectral boundary. We reformulated the ASEP generator matrices as non-Hermitian fermionic models with a variable interaction parameter U, where $U = 1$ corresponds to the standard ASEP. We analytically demonstrated that in the noninteracting ASEP ($U = 0$), this spiky spectral boundary arises from aggregating single-particle eigenvalues positioned on ellipses (circles for TASEP). For PBCs, we extended this concept to interacting TASEP, showing that the spiky boundary remains and originates from the summation of clustered Bethe roots. Lastly, we confirmed the robustness of this spiky boundary by considering only the cycle structure in the many-body graph, revealing that corresponding random graphs exhibit a similar spiky spectral boundary.

This research opens up several questions for further exploration. We demonstrated the spiky spectral boundary in TASEP, largely attributed to Bethe roots clustering. It is intriguing to consider whether such clustering also occurs in ASEP. The straightforward connection between TASEP and ASEP in their noninteracting forms suggests that the spiky spectral boundary might extend to standard ASEP (with $U = 1$) as well. However, it remains to be seen how introducing interactions influences Bethe roots clustering and the potential emergence of a spiky spectral boundary.

In this paper, we concentrated on the Bethe ansatz for PBCs. The ASEP with OBCs is also solvable via the Bethe ansatz, though the equations are more complex, as detailed in various studies [81,101–104]. One might ask whether the spiky spectral boundary in the OBC case is also associated with a clustering of Bethe roots similar to the PBC case.

The spectral boundary of random graphs with dominant cycle lengths typically follows a hypotrochoidic curve, as noted in Ref. [37]. These graphs usually lack cycles shorter than L but can have cycles longer than L. However, the random graph ensemble we introduced deviates from this standard hypotrochoidic pattern, likely due to its more restricted cycle structure, where all cycles are of lengths divisible by L. Extending the hypotrochoidic law to encompass this specific graph ensemble would be a valuable advancement.

This paper concentrated on the spiky spectral boundary of the ASEP. Formation of spikes has as well been observed in the off-diagonals of reduced density matrices in the symmetric simple exclusion process (XXX model) [105] and the observable representation of Ising chain Glauber dynamics [106]. These observations together with the robustness of the spiky spectral boundary to perturbations make the investigation of other models, both classical and quantum, that possess a similar cycle structure in their many-body graphs or comparable trace correlations in their generator matrices, an intriguing direction for future research.

APPENDIX A: QUADRATIC FERMION MODEL FOR OBC

In this Appendix, we will show that the noninteracting ASEP H_0 with OBC is a quadratic fermion model. Especially, we will prove Eq. (11).

Recall

$$H_0 = \sum_{j=1}^{L-1}(p\sigma_{j+1}^+\sigma_j^- + q\sigma_j^+\sigma_{j+1}^-) + \alpha\sigma_1^+ + \gamma\sigma_1^-$$
$$+ \beta\sigma_L^- + \delta\sigma_L^+. \tag{A1}$$

For that, we first apply, as mentioned in the main text, the Kramers-Wannier duality transformation [36]

$$\sigma_j^x \rightarrow \prod_{l=1}^{j}\sigma_l^z, \quad \sigma_j^z \rightarrow \sigma_j^x\sigma_{j+1}^x, \tag{A2}$$

where we implicitly have enlarged the chain of length L by one additional site to a chain of length $L+1$. Thus, the multiplicity of every eigenvalue of the so-transformed H_0 is doubled. Applying a Jordan-Wigner transformation

$$w_j = \left(\prod_{l=1}^{j-1}\left(-\sigma_l^z\right)\right)\sigma_j^-, \quad w_j^\dagger = \left(\prod_{l=1}^{j-1}\left(-\sigma_l^z\right)\right)\sigma_j^+, \tag{A3}$$

and rewriting in terms of Majorana real and imaginary parts of the Dirac fermions $w, w^\dagger$,

$$\gamma_{j,1} = w_j^\dagger + w_j, \quad \gamma_{j,2} = i(w_j^\dagger - w_j), \tag{A4}$$

the Hamiltonian H_0 is given by

$$H_0 = \sum_{j=1}^{L-1}\left[\frac{p+q}{4}(i\gamma_{j+1,1}\gamma_{j+1,2} - i\gamma_{j,2}\gamma_{j+2,1}) + \frac{p-q}{4}(\gamma_{j+1,1}\gamma_{j+2,1} + \gamma_{j,2}\gamma_{j+1,2})\right]$$

$$+ \frac{1}{2}[(\alpha+\gamma)i\gamma_{1,1}\gamma_{1,2} + (\alpha-\gamma)\gamma_{1,1}\gamma_{2,1}] + \frac{1}{2}\left(\prod_{j=1}^{L+1}i\gamma_{j,1}\gamma_{j,2}\right)[(\delta+\beta)i\gamma_{L+1,1}\gamma_{L+1,2} - (\delta-\beta)\gamma_{L,2}\gamma_{L+1,2}]. \tag{A5}$$

The string of Majoranas $\prod_{j=1}^{L+1}(i\gamma_{j,1}\gamma_{j,2}) = (-1)^{L+1}\mathcal{P}_w$ equals, up to a sign, the parity operator $\mathcal{P}_w$ of Dirac fermions $w, w^\dagger$, which commutes with H_0. Thus, restricted to the subspaces of constant parity, the Hamiltonian H_0 becomes quadratic.

Note that H_0 in terms of the Majorana fermions $\gamma_{j,l}$ is acting nontrivially on the additional site $L+1$.

To keep the algebra simpler, let us consider from now on the case $p=1$ and $q=\gamma=\delta=0$. The following calculations can be straightforwardly generalized to arbitrary p, q, γ, δ. Thus, H_0 in terms of the Majorana fermions γ simplifies to

$$H_0 = \sum_{j=1}^{L-1}(\sigma_{j+1}^+\sigma_j^-) + \alpha\sigma_1^+ + \beta\sigma_L^-$$

$$= \frac{1}{2}\alpha[i\gamma_{1,1}\gamma_{1,2} + \gamma_{1,1}\gamma_{2,1}] + \frac{1}{2}(-1)^{L+1}\mathcal{P}_w\beta[i\gamma_{L+1,1}\gamma_{L+1,2} + \gamma_{L,2}\gamma_{L+1,2}] + \frac{1}{4}\sum_{j=1}^{L-1}\left[(\gamma_{j,2}, \ \gamma_{j+1,1})\begin{pmatrix}1 & -i\\ i & 1\end{pmatrix}\begin{pmatrix}\gamma_{j+1,2}\\ \gamma_{j+2,1}\end{pmatrix}\right]. \tag{A6}$$

The eigenvalues of the 2×2-matrix are 0 and 2, while the eigenvectors are $(1, -i)^t$ and $(1, i)^t$, respectively. Thus, the following pairing of Majorana fermions:

$$c_j^\dagger = \tfrac{1}{2}(\gamma_{j,2} - i\gamma_{j+1,1}), \quad c_j = \tfrac{1}{2}(\gamma_{j,2} + i\gamma_{j+1,1}), \quad (A7)$$

into Dirac fermions $c, c^\dagger$ drastically simplifies the bulk term. By identifying $\gamma_{L+2,1} = \gamma_{1,1}$ the pairing given by Eqs. (A7) turns the chain on sites 1 to $L + 1$ into a ring, connecting site 1 and $L + 1$. The Hamiltonian H_0 is given in terms of $c, c^\dagger$ as

$$H_0 = \alpha(c_{L+1} - c_{L+1}^\dagger)c_1^\dagger + \sum_{j=1}^{L-1}[c_j c_{j+1}^\dagger]$$

$$+ (-1)^L \mathcal{P}_c \beta c_L(c_{L+1} + c_{L+1}^\dagger),$$

where $\mathcal{P}_c$ denotes the parity of the Dirac fermions $c, c^\dagger$. This is Eq. (11).

APPENDIX B: DIAGONALIZING M_c

In this Appendix, we calculate the eigenvalues and eigenvectors of M_c given by Eq. (30) and Eqs. (31)–(33) thereafter. We denote the eigenvalue equation by $M_c \boldsymbol{u} = \lambda \boldsymbol{u}$ with the $2L + 2$ dimensional vector $\boldsymbol{u}$. In terms of $\boldsymbol{u} = (u_1, \ldots, u_{L+1}, u_1', \ldots, u_{L+1}')$, the eigenvalue equation reads

$$\lambda u_1 = -\alpha(u_{L+1} - u_{L+1}'), \quad (B1)$$

$$\lambda u_2 = -u_1, \quad (B2)$$

$$\cdots$$

$$\lambda u_{L-1} = -u_{L-2}, \quad (B3)$$

$$\lambda u_L = -u_{L-1}, \quad (B4)$$

$$\lambda u_{L+1} = -s\beta u_L - \alpha u_1', \quad (B5)$$

and

$$\lambda u_1' = u_2', \quad (B6)$$

$$\lambda u_2' = u_3', \quad (B7)$$

$$\cdots$$

$$\lambda u_{L-1}' = u_L', \quad (B8)$$

$$\lambda u_L' = \beta s(u_{L+1} + u_{L+1}'), \quad (B9)$$

$$\lambda u_{L+1}' = -\beta s u_L + \alpha u_1'. \quad (B10)$$

Combining Eqs. (B2)–(B4) with $u_1, \ldots, u_L$ and Eqs. (B6)–(B8) with $u_1', \ldots, u_L'$ recursively, we get for $2 \leqslant j \leqslant L$:

$$u_j = -\lambda^{-1} u_{j-1} = \cdots = (-\lambda)^{-j+1} u_1 \quad (B11)$$

and

$$u_j' = \lambda u_{j-1}' = \cdots = \lambda^{j-1} u_1'. \quad (B12)$$

Especially, the following holds:

$$u_L = (-\lambda)^{-L+1} u_1, \quad (B13)$$

$$u_L' = \lambda^{L-1} u_1'. \quad (B14)$$

By substituting Eqs. (B13) and (B14) into Eqs. (B5) and (B10), respectively, we get

$$u_1 = \alpha\lambda^{-1}(-u_{L+1} + u_{L+1}'), \quad (B15)$$

$$u_{L+1} = \beta s(-\lambda)^{-L} u_1 - \alpha\lambda^{-1} u_1', \quad (B16)$$

$$u_1' = \lambda^{-L} \beta s(u_{L+1} + u_{L+1}'), \quad (B17)$$

$$u_{L+1}' = \beta s(-\lambda)^{-L} u_1 + \alpha\lambda^{-1} u_1'. \quad (B18)$$

Adding and subtracting Eqs. (B16) and (B18), respectively, leads to

$$u_{L+1} + u_{L+1}' = 2\beta s(-\lambda)^{-L} u_1 \quad (B19)$$

$$-u_{L+1} + u_{L+1}' = 2\alpha\lambda^{-1} u_1', \quad (B20)$$

which, in turn, implies that

$$u_1' = 2(-1)^L \lambda^{-2L} \beta^2 u_1, \quad (B21)$$

$$u_1 = 2\alpha^2 \lambda^{-2} u_1', \quad (B22)$$

by using Eqs. (B15) and (B17). Combining the last two equations leads to

$$u_1 = 4(\alpha\beta)^2(-1)^L \lambda^{-2L-2} u_1, \quad (B23)$$

which implies, for $u_1 \neq 0$, the eigenvalue Eq. (35):

$$\lambda^{2(L+1)} = (-1)^L 4(\alpha\beta)^2. \quad (B24)$$

The roots of this polynomial are given by

$$\lambda = (2\alpha\beta)^{\frac{1}{L+1}} \begin{cases} \exp\left(\frac{i\pi}{2L+2}2k\right) & L \text{ even} \\ \exp\left(\frac{i\pi}{2L+2}(2k-1)\right) & L \text{ odd}, \end{cases}$$

where $k = 1, \ldots, 2L + 2$.

APPENDIX C: BETHE EQUATIONS FOR PBC ASEP WITH ARBITRARY U

In this Appendix, we derive the Bethe equations presented in Sec. V A. These results extend the usual $U = 1$ ASEP Bethe ansatz [32] to the case of arbitrary U. In different notations, such deformations have appeared in Refs. [41,92].

By $|x_1, \ldots, x_N\rangle$, we denote the state of N particles at positions $x_1, \ldots, x_N$. In the following, we let $x_1 < \cdots < x_N$ up to an overall shift in the indices. The wave function $|\psi\rangle$ in the basis of $|x_1, \ldots, x_N\rangle$ is given by

$$|\psi\rangle = \sum_{x_1 < \cdots < x_N} \psi(x_1, \ldots, x_N)|x_1, \ldots, x_N\rangle, \quad (C1)$$

where $\psi(x_1, \ldots, x_N)$ denotes the coefficient of $|\psi\rangle$ with respect to $|x_1, \ldots, x_N\rangle$. Now, let $|\psi\rangle$ be an eigenstate of the generalized Markov matrix H with eigenvalue E, i.e., $H|\psi\rangle = E|\psi\rangle$. Recall that we can write the generator matrix H as

$$H = \sum_{i=1}^{L} (p\sigma_i^- \sigma_{i+1}^+ + q\sigma_i^+ \sigma_{i+1}^-) + \frac{U}{4} \sum_{i=1}^{L} (\sigma_i^z \sigma_{i+1}^z - 1). \tag{C2}$$

Let us first focus on the action of the off-diagonal term in Eq. (C2) on $|x_1, \ldots, x_N\rangle$. It is easy to see that

$$\sum_{i=1}^{L-1} \sigma_i^- \sigma_{i+1}^+ |x_1, \ldots, x_N\rangle = \sum_{j=1}^{N-1} (1 - \delta(x_{j+1} - x_j, 1))|x_1, \ldots, x_j + 1, \ldots, x_N\rangle \tag{C3}$$

and

$$\sum_{i=1}^{L-1} \sigma_i^+ \sigma_{i+1}^- |x_1, \ldots, x_N\rangle = \sum_{j=2}^{N} (1 - \delta(x_j - x_{j-1}, 1))|x_1, \ldots, x_j - 1, \ldots, x_N\rangle, \tag{C4}$$

where $\delta(x, y)$ equals one whenever $x = y$ and is zero otherwise. The remaining boundary terms are determined as follows. If $x_N \neq L$, then $\sigma_L^- \sigma_1^+ |x_1, \ldots, x_N\rangle = 0$, so let $x_N = L$. Then

$$\sigma_L^- \sigma_1^+ |x_1, \ldots, x_N\rangle = (1 - \delta(x_1, 1))|1, x_1, \ldots, x_{N-1}\rangle \tag{C5}$$

$$= (1 - \delta(x_1 - x_N \bmod L, 1))|x_1, \ldots, x_{N-1}, X_N + 1\rangle \tag{C6}$$

by identifying $|x_1, \ldots, x_{N-1}, L+1\rangle = |1, x_1, \ldots, x_{N-1}\rangle$. On the other hand, whenever $x_1 \neq 1$ we have $\sigma_L^+ \sigma_1^- |x_1, \ldots, x_N\rangle = 0$, while for $x_1 = 1$ we get

$$\sigma_L^+ \sigma_1^- |x_1, \ldots, x_N\rangle = (1 - \delta(x_N, L))|x_2, \ldots, x_N, L\rangle \tag{C7}$$

$$= (1 - \delta(x_1 - x_N \bmod L, 1))|x_1 - 1, x_2, \ldots, x_N\rangle, \tag{C8}$$

where we identified $|x_2, \ldots, x_N, L\rangle = |0, x_2, \ldots, x_N\rangle$. Taking everything together, we have

$$\sum_{i=1}^{L} \sigma_i^- \sigma_{i+1}^+ |x_1, \ldots, x_N\rangle = \sum_{j=1}^{N} (1 - \delta(x_{j+1} - x_j \bmod L, 1))|x_1, \ldots, x_j + 1, \ldots, x_N\rangle, \tag{C9}$$

$$\sum_{i=1}^{L} \sigma_i^+ \sigma_{i+1}^- |x_1, \ldots, x_N\rangle = \sum_{j=1}^{N} (1 - \delta(x_j - x_{j-1} \bmod L, 1))|x_1, \ldots, x_j - 1, \ldots, x_N\rangle. \tag{C10}$$

The diagonal term in Eq. (C2) acts on $|x_1, \ldots, x_N\rangle$ as

$$\frac{1}{4} \sum_{i=1}^{L} (\sigma_i^z \sigma_{i+1}^z - 1)|x_1, \ldots, x_N\rangle = \sum_{j=1}^{N-1} (\delta(x_{j+1} - x_j, 1) + \delta(x_1 - x_N, 1 - L) - 1)|x_1, \ldots, x_N\rangle$$

$$= \sum_{j=1}^{N} (\delta(x_{j+1} - x_j \bmod L, 1) - 1)|x_1, \ldots, x_N\rangle, \tag{C11}$$

where we note that $\sigma_i^z = 2n_i - 1$ and thus

$$\frac{1}{4} \sum_{i=1}^{L} (\sigma_i^z \sigma_{i+1}^z - 1) = \frac{4}{4} \sum_{i=1}^{L} n_i n_{i+1} - \frac{2}{4} \sum_{i=1}^{L} n_i - \frac{2}{4} \sum_{i=1}^{L} n_{i+1} = \left[\sum_{i=1}^{L} n_i n_{i+1}\right] - N. \tag{C12}$$

Summarizing, the action of H on $|x_1, \ldots, x_N\rangle$ is

$$H|x_1, \ldots, x_N\rangle = p \sum_{j=1}^{N} (1 - \delta(x_{j+1} - x_j \bmod L, 1))|x_1, \ldots, x_j + 1, \ldots, x_N\rangle$$

$$+ q \sum_{j=1}^{N} (1 - \delta(x_j - x_{j-1} \bmod L, 1))|x_1, \ldots, x_j - 1, \ldots, x_N\rangle$$

$$- U \sum_{j=1}^{N} (1 - \delta(x_{j+1} - x_j \bmod L, 1))|x_1, \ldots, x_N\rangle. \tag{C13}$$

Now, consider the eigenvalue equation $H|\psi\rangle = E|\psi\rangle$:

$$H|\psi\rangle = \sum_{x_1 < \cdots < x_N} \psi(x_1, \ldots, x_N) H|x_1, \ldots, x_N\rangle = \sum_{x_1 < \cdots < x_N} \psi(x_1, \ldots, x_N) E|x_1, \ldots, x_N\rangle. \tag{C14}$$

Let us concentrate on the term in Eq. (C13) proportional to p:

$$p \sum_{j=1}^{N} \sum_{x_1 < \cdots < x_N} \psi(x_1, \ldots, x_N)(1 - \delta(x_{j+1} - x_j \bmod L, 1))|x_1, \ldots, x_j + 1, \ldots, x_N\rangle. \tag{C15}$$

After a change of variables $\tilde{x}_i = x_i$ for $i \neq j$ and $\tilde{x}_j = x_j + 1$, the above equation reads

$$p \sum_{j=1}^{N} \sum_{\tilde{x}_1 < \cdots < \tilde{x}_N} \psi(\tilde{x}_1, \ldots, \tilde{x}_j - 1, \ldots, \tilde{x}_N)(1 - \delta(\tilde{x}_j - \tilde{x}_{j-1} \bmod L, 1))|\tilde{x}_1, \ldots, \tilde{x}_N\rangle. \tag{C16}$$

Let us now focus on the term in Eq. (C13) proportional to q. One finds with the change $\tilde{x}_j = x_j - 1 < x_{j+1} - 1 = \tilde{x}_{j+1} - 1$, thus $\tilde{x}_{j+1} - \tilde{x}_j > 1$ and $\tilde{x}_{j-1} = x_{j-1} < x_j - 1 = \tilde{x}_j$, that this term equals

$$q \sum_{\tilde{x}_1 < \cdots < \tilde{x}_N} \psi(\tilde{x}_1, \ldots, \tilde{x}_j + 1, \ldots, \tilde{x}_N)(1 - \delta(\tilde{x}_{j+1} - \tilde{x}_j \bmod L, 1))|\tilde{x}_1, \ldots, \tilde{x}_N\rangle, \tag{C17}$$

where the first constraint is realized via the delta term and the second constraint by the summation.

By orthogonality of $|x_1, \ldots, x_N\rangle$, the eigenvalue equation $H|\psi\rangle = E|\psi\rangle$ turns into $\binom{L}{N}$ equations for the wave-function coefficients:

$$p \sum_{j=1}^{N} (1 - \delta(x_j - x_{j-1} \bmod L, 1))(\psi(x_1, \ldots, x_j - 1, \ldots, x_N) - U\psi(x_1, \ldots, x_N))$$

$$+ q \sum_{j=1}^{N} (1 - \delta(x_{j+1} - x_j \bmod L, 1))(\psi(x_1, \ldots, x_j + 1, \ldots, x_N) - U\psi(x_1, \ldots, x_N))$$

$$= E\psi(x_1, \ldots, x_N). \tag{C18}$$

Here we additionally used that $p + q = 1$. Now, we make the ansatz for the wave-function coefficient

$$\psi(x_1, \ldots, x_N) = \sum_{\tau \in S_N} A(\tau) \prod_{j=1}^{N} z_{\tau(j)}^{x_j}, \tag{C19}$$

where the summation runs over all elements of the symmetric group S_N and the z_j's and $A(\tau)'$s are complex numbers. Let us consider a configuration $x_1 < \cdots < x_N$ where all particles have at least distance 1, i.e., no consecutive particles. Plugging the ansatz into the term proportional to p results in

$$\sum_{j=1}^{N} \psi(x_1, \ldots, x_j - 1, \ldots, x_N) - U\psi(x_1, \ldots, x_N) = \sum_{j=1}^{N} \sum_{\tau \in S_N} A(\tau) \left(z_{\tau(j)}^{x_j - 1} \prod_{l=1; l \neq j}^{N} z_{\tau(l)}^{x_l} - U \prod_{l=1}^{N} z_{\tau(l)}^{x_l} \right) \tag{C20}$$

$$= \sum_{\tau \in S_N} A(\tau) \prod_{l=1}^{N} z_{\tau(l)}^{x_l} \sum_{j=1}^{N} (z_{\tau(j)}^{-1} - U). \tag{C21}$$

Similarly, one gets the analogous expression for the term proportional to q with the change $z_{\tau(j)}^{-1} \rightarrow z_{\tau(j)}$. Thus, Eq. (C18) in terms of the Bethe ansatz reads

$$E = \sum_{j=1}^{N} (q z_j + p z_j^{-1} - U), \tag{C22}$$

which is Eq. (49) in Sec. V A. Now, consider a configuration $|x_1, \ldots, x_N\rangle$ with two particles adjacent to each other. Then, for $1 \leqslant l, k \leqslant N$, it holds that

$$A(\ldots, l, \ldots, k, \ldots) = -\frac{p + q z_l z_k - U z_l}{p + q z_l z_k - U z_k} A(\ldots, k, \ldots, l, \ldots). \tag{C23}$$

The periodic boundary condition enforces $\psi(x_1, \ldots, x_{N-1}, L + 1) = \psi(1, x_1, \ldots, x_{N-1})$, which implies

$$A(\tau(1), \ldots, \tau(N)) z_{\tau(N)}^{L} = A(\tau(N), \tau(1), \ldots, \tau(N-1)). \tag{C24}$$

Combining both constraints leads to the Bethe equations

$$z_j^L = \prod_{k=1; k \neq j}^N \left(-\frac{p + q z_j z_k - U z_j}{p + q z_j z_k - U z_k} \right). \tag{C25}$$

In the case of TASEP with $q = 1$ and $p = 0$ the Bethe equations reduce to

$$z_j^L = \prod_{k=1; k \neq j}^N \left(-\frac{z_j z_k - U z_j}{z_j z_k - U z_k} \right) = \frac{z_j^N}{(z_j - U)^N} (-1)^{N-1} \prod_{k=1}^N \frac{z_k - U}{z_k}, \tag{C26}$$

so

$$z_j^{L-N} (z_j - U)^N = (-1)^{N-1} \prod_{k=1}^N \frac{z_k - U}{z_k}. \tag{C27}$$

Denoting $Z_k = 2 z_k - U$ we get

$$(U + Z_j)^{L-N} (U - Z_j)^N = -2^L \prod_{k=1}^N \frac{Z_k - U}{Z_k + U}. \tag{C28}$$

APPENDIX D: SOLVING THE BETHE EQUATIONS NUMERICALLY

In this Appendix, we will describe how to self-consistently solve the Bethe equations numerically. We will mostly follow the approach in Ref. [9] with some additional tweaks.

Restricting to $p = 1$ and $q = 0$ reduces the difficulty of solving the Bethe equations considerably because the right-hand side of Eq. (52) does not depend on j, as does the right-hand side of Eq. (50) for general p, q.

Consider the polynomial $P(z)$,

$$P(z) = (U + z)^{L-N} (U - z)^N - Y, \tag{D1}$$

where Y denotes an arbitrary complex number and let us denote the right-hand side of Eq. (52) by

$$\tilde{Y}(Z_1, \ldots, Z_N) = 2^L \prod_{k=1}^N \frac{Z_k - U}{Z_k + U}. \tag{D2}$$

Then every solution $Z_1, \ldots, Z_N$ of Eq. (52) are roots of the polynomial P with $Y = \tilde{Y}(Z_1, \ldots, Z_N)$. To find a solution to the Bethe equations, one first calculates the roots $Z_1^{(1)}, \ldots, Z_L^{(1)}$ of P for an initial $Y^{(1)}$. Of these L roots of P, one chooses N roots, $Z_1^{(1)}, \ldots, Z_N^{(1)}$, and evaluates the next $Y^{(2)} = \tilde{Y}(Z_1^{(1)}, \ldots, Z_N^{(1)})$. Again, the roots $Z_1^{(2)}, \ldots, Z_L^{(2)}$ of P with $Y = Y^{(2)}$ are calculated and N roots $Z_1^{(1)}, \ldots, Z_N^{(1)}$ are chosen to evaluate the next $Y^{(3)} = \tilde{Y}(Z_1^{(2)}, \ldots, Z_N^{(2)})$. This procedure is then iterated until convergence all of the N chosen roots is reached, $Z_j^{(l)} \approx Z_j^{(l+1)}$ for all $1 \leqslant j \leqslant N$.

The convergence of this procedure presupposes consistency of the choice of the N roots out of L roots of the polynomial P [34,51]. The first choice of $Z_1^{(1)}, \ldots, Z_N^{(1)}$ out of $Z_1^{(1)}, \ldots, Z_L^{(1)}$ is arbitrary. Subsequent roots $Z_1^{(l)}, \ldots, Z_N^{(l)}$ are chosen to be closest to the previous roots,

$$Z_j^{(l)} = \operatorname*{argmin}_{Z_k^{(l)}: 1 \leqslant k \leqslant L} \left| Z_k^{(l)} - Z_j^{(l-1)} \right|, \tag{D3}$$

where the minimum runs over all roots $Z_1^{(l)}, \ldots, Z_L^{(l)}$ of P with $Y = Y^{(l)}$. If multiple $Z_k^{(l)}$ are close to $Z_j^{(l-1)}$ we do not update $Y^{(l+1)}$ with $Z_j^{(l)}$ but with a linear combination of $Z_j^{(l)}$ and $Z_j^{(l-1)}$, i.e., $Y^{(l+1)} = \tilde{Y}(\ldots, dY\ Z_j^{(l)} + (1 - dY) Z_j^{(l-1)}, \ldots)$, where $0 < dY \leqslant 1$ denotes the fraction of interpolation between $Z_j^{(l)}$ and $Z_j^{(l-1)}$.

The above-described procedure typically leads to convergence of $Z_1^{(l)}, \ldots, Z_N^{(l)}$ and thus to a solution of the Bethe Eqs. (52). In Fig. 9, we show the roots $Z_1^{(l)}, \ldots, Z_6^{(l)}$ obtained during the above algorithm for $L = 6$ and $N = 3$. The square markers denote the initial $Z_1^{(1)}, \ldots, Z_6^{(1)}$ with $Y^{(1)} = 10 \times 2^L$, while the triangles denote the final and converged $Z_1^{(\text{end})}, \ldots, Z_6^{(\text{end})}$ [relative or absolute error of Eq. (52) $< 10^{-3}$]. The circles indicate intermediate roots.
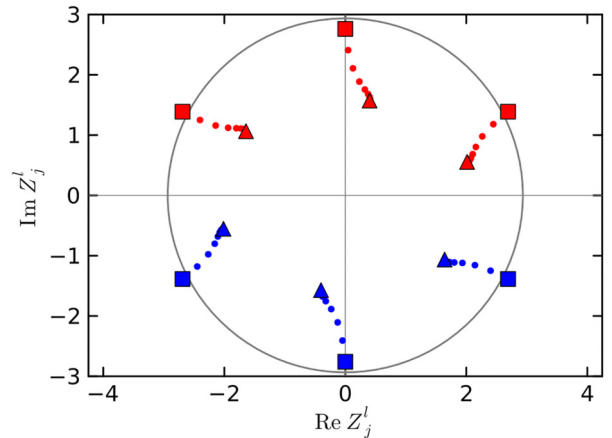

FIG. 9. Visualization of solving the Bethe Eqs. (52) of TASEP (PBCs) for $L = 6$ and $N = 3$. All markers are roots of the polynomial P [Eq. (D1)] for different Y. The outer (square) markers are the roots for initial $Y^{(1)} = 10 \times 2^L$, the inner (triangles) markers for Y converged, and the circles denote roots of P for intermediate Y. Red markers (upper complex plane) are chosen to calculate the next Y. Gray circle has radius $|Y^{(1)}|^{1/L}$.

Initially, the three red squares (upper half-plane) are chosen as $Z_1^{(1)}, \ldots, Z_3^{(1)}$ and subsequent roots (upper half-plane in red) according to their previous closest roots. For visualization purposes, dY was chosen to be $dY = 0.5$.

To find all solutions to the Bethe Eqs. (52) systematically, we use different combinations of initial $Y^{(1)}$ and initial root choices, namely, we typically choose $Y^{(1)}$ with $|Y^{(1)}|^{1/L} \gg U$. This ensures that the roots of P with $Y = Y^{(1)}$ are close to the circle with radius $|Y^{(1)}|^{1/L}$. In Fig. 9, the roots of P for $Y = Y^{(1)} = 10 \times 2^6$ denoted by the square markers are close to the circle with radius $2 \times 10^{1/6} \approx 2.9$. Then we solve the Bethe equations for every combination of N roots out of L. This typically gives us almost all solutions of the Bethe Eqs. (52). By iterating this procedure for a handful of initial $Y^{(1)}$, we found all Bethe roots for the systems we investigated (up to $L = 22$).

APPENDIX E: PROOF THAT CYCLE LENGTHS OF GRAPHS IN SEC. VI ARE DIVISIBLE BY L

In this Appendix, we will show that all cycle lengths of the random graphs introduced in Sec. VI are divisible by L.

We label the vertices $\{1, \ldots, D\}$ and assign to each edge $e = (i, j)$ the integer

$$n(e) = n((i, j)) = j - i. \qquad (E1)$$

We argue that all cycle lengths of our random graphs are divisible by L in two steps. First, we will show that the random graphs have the property that

$$n(e) \bmod L = 1 \quad \text{for all edges } e. \qquad (E2)$$

Second, we will prove that cycle lengths in graphs with such a property are divisible by L.

The random graphs in Sec. VI are sampled by initially considering a single (Hamiltonian) cycle on D vertices. Without loss of generality, we label the vertices such that the edges are given by $e = (i, i + 1)$ for $1 \leqslant i < D$ and $e = (D, 1)$. In the former case, $n(e) = 1$, and in the latter case, $n(e) \bmod L = 1$ whenever $D \bmod L = 0$. Hence, this initial graph obeys the property in Eq. (E2).

Next, we will argue that Eq. (E2) holds for newly added edges e_L. Such edges $e_L = (j, i)$ are constructed by choosing an arbitrary initial vertex i and traversing along a path $(e_1, \ldots, e_{L-1})$ in the graph to an ending vertex j. Since $e_1, \ldots, e_{L-1}$ obey Eq. (E2), we let $n(e_s) = n_s + 1$ with $n_s \bmod L = 0$. Consequently,

$$n(e_L) = -\sum_{s=1}^{L-1} (n_s + 1) = -\left(\sum_{s=1}^{L-1} n_s\right) - L + 1, \qquad (E3)$$

and the added edge e_L obeys Eq. (E2) as well. We therefore have established that the random graphs in Sec. VI obey Eq. (E2).

To conclude our argument that all cycle lengths are divisible by L, we consider an arbitrary cycle $(e_1, \ldots, e_l)$ of length l in a graph that obeys Eq. (E2). For $n(e_s) = n_s + 1$ with $n_s \bmod L = 0$, it holds that

$$0 = \sum_{s=1}^{l} (n_s + 1) = \left(\sum_{s=1}^{l} n_s\right) + l. \qquad (E4)$$

Since the sum in Eq. (E4) is divisible by L, so must l. This concludes our proof that all cycle lengths of the graphs in Sec. VI are divisible by L.

[1] F. Spitzer, Interaction of Markov processes, Adv. Math. **5**, 246 (1970).

[2] T. M. Liggett, *Interacting Particle Systems* (Springer, New York, 1985), Vol. 2.

[3] H. Spohn, *Large Scale Dynamics of Interacting Particles* (Springer, Berlin, Heidelberg, 1991).

[4] G. Schütz and E. Domany, Phase transitions in an exactly soluble one-dimensional exclusion process, J. Stat. Phys. **72**, 277 (1993).

[5] B. Derrida, M. R. Evans, V. Hakim, and V. Pasquier, Exact solution of a 1D asymmetric exclusion model using a matrix formulation, J. Phys. A: Math. Gen. **26**, 1493 (1993).

[6] B. Derrida, An exactly soluble non-equilibrium system: The asymmetric simple exclusion process, Phys. Rep. **301**, 65 (1998).

[7] T. M. Liggett, *Stochastic Interacting Systems: Contact, Voter and Exclusion Processes* (Springer, Berlin, Heidelberg, 1999), Vol. 324.

[8] G. M. Schütz, Exactly solvable models for many-body systems far from equilibrium, Phase Transitions Crit. Phenom. **19**, 1 (2001).

[9] O. Golinelli and K. Mallick, The asymmetric simple exclusion process: An integrable model for non-equilibrium statistical mechanics, J. Phys. A: Math. Gen. **39**, 12679 (2006).

[10] T. Chou, K. Mallick, and R. K. P. Zia, Non-equilibrium statistical mechanics: from a paradigmatic model to biological transport, Rep. Prog. Phys. **74**, 116601 (2011).

[11] K. Mallick, The exclusion process: A paradigm for non-equilibrium behaviour, Physica A **418**, 17 (2015).

[12] J. Krug, Boundary-induced phase transitions in driven diffusive systems, Phys. Rev. Lett. **67**, 1882 (1991).

[13] T. Sasamoto, One-dimensional partially asymmetric simple exclusion process with open boundaries: Orthogonal polynomials approach, J. Phys. A: Math. Gen. **32**, 7109 (1999).

[14] R. A. Blythe, M. R. Evans, F. Colaiori, and F. H. L. Essler, Exact solution of a partially asymmetric exclusion model using a deformed oscillator algebra, J. Phys. A: Math. Gen. **33**, 2313 (2000).

[15] A. Parmeggiani, T. Franosch, and E. Frey, Phase coexistence in driven one-dimensional transport, Phys. Rev. Lett. **90**, 086601 (2003).

[16] R. A. Blythe and M. R. Evans, Nonequilibrium steady states of matrix-product form: A solver's guide, J. Phys. A: Math. Theor. **40**, R333 (2007).

[17] B. Derrida, S. A. Janowsky, J. L. Lebowitz, and E. R. Speer, Exact solution of the totally asymmetric simple exclusion process: Shock profiles, J. Stat. Phys. **73**, 813 (1993).

[18] K. Mallick, Shocks in the asymmetry exclusion model with an impurity, J. Phys. A: Math. Gen. **29**, 5375 (1996).

[19] F. H. Jafarpour, Multiple shocks in a driven diffusive system with two species of particles, Physica A **358**, 413 (2005).

[20] M. Kim, L. Santen, and J. D. Noh, Asymmetric simple exclusion process in one-dimensional chains with long-range links, J. Stat. Mech.: Theory Exp. (2011) P04003.

[21] C. Arita, Synchronized shocks in an inhomogeneous exclusion process, Europhys. Lett. **112**, 40001 (2015).

[22] C. T. MacDonald and J. H. Gibbs, Concerning the kinetics of polypeptide synthesis on polyribosomes, Biopolymers **7**, 707 (1969).

[23] C. T. MacDonald, J. H. Gibbs, and A. C. Pipkin, Kinetics of biopolymerization on nucleic acid templates, Biopolymers **6**, 1 (1968).

[24] P. C. Bressloff and J. M. Newby, Stochastic models of intracellular transport, Rev. Mod. Phys. **85**, 135 (2013).

[25] I. Neri, N. Kern, and A. Parmeggiani, Modeling cytoskeletal traffic: An interplay between passive diffusion and active transport, Phys. Rev. Lett. **110**, 098102 (2013).

[26] X. Fang, K. Kruse, T. Lu, and J. Wang, Nonequilibrium physics in biology, Rev. Mod. Phys. **91**, 045004 (2019).

[27] D. Helbing, Traffic and related self-driven many-particle systems, Rev. Mod. Phys. **73**, 1067 (2001).

[28] T. Karzig and F. Von Oppen, Signatures of critical full counting statistics in a quantum-dot chain, Phys. Rev. B **81**, 045317 (2010).

[29] P. Meakin, P. Ramanlal, L. M. Sander, and R. C. Ball, Ballistic deposition on surfaces, Phys. Rev. A **34**, 5091 (1986).

[30] M. Kardar, G. Parisi, and Y.-C. Zhang, Dynamic scaling of growing interfaces, Phys. Rev. Lett. **56**, 889 (1986).

[31] J. Krug and H. Spohn, Kinetic roughening of growing surfaces, in *Solids Far From Equilibrium* (Cambridge University Press, Cambridge, 1991), p. 479.

[32] L. H. Gwa and H. Spohn, Bethe solution for the dynamical-scaling exponent of the noisy Burgers equation, Phys. Rev. A **46**, 844 (1992).

[33] S. Prolhac, Spectrum of the totally asymmetric simple exclusion process on a periodic lattice-bulk eigenvalues, J. Phys. A: Math. Theor. **46**, 415001 (2013).

[34] S. Prolhac, Current fluctuations and large deviations for periodic TASEP on the relaxation scale, J. Stat. Mech.: Theory Exp. (2015) P11028.

[35] F. H. L. Essler and V. Rittenberg, Representations of the quadratic algebra and partially asymmetric diffusion with open boundaries, J. Phys. A: Math. Gen. **29**, 3375 (1996).

[36] J. B. Kogut, An introduction to lattice gauge theory and spin systems, Rev. Mod. Phys. **51**, 659 (1979).

[37] P. V. Aceituno, T. Rogers, and H. Schomerus, Universal hypotrochoidic law for random matrices with cyclic correlations, Phys. Rev. E **100**, 010302 (2019).

[38] T. Prosen, Third quantization: a general method to solve master equations for quadratic open Fermi systems, New J. Phys. **10**, 043026 (2008).

[39] D. Dhar, An exactly solved model for interfacial growth, Phase Transitions **9**, 51 (1987).

[40] D. Kim, Bethe ansatz solution for crossover scaling functions of the asymmetric XXZ chain and the Kardar-Parisi-Zhang-type growth model, Phys. Rev. E **52**, 3512 (1995).

[41] B. Derrida and J. L. Lebowitz, Exact large deviation function in the asymmetric exclusion process, Phys. Rev. Lett. **80**, 209 (1998).

[42] O. Golinelli and K. Mallick, Bethe ansatz calculation of the spectral gap of the asymmetric exclusion process, J. Phys. A: Math. Gen. **37**, 3321 (2004).

[43] O. Golinelli and K. Mallick, Hidden symmetries in the asymmetric exclusion process, J. Stat. Mech.: Theory Exp. (2004) P12001.

[44] O. Golinelli and K. Mallick, Spectral gap of the totally asymmetric exclusion process at arbitrary filling, J. Phys. A: Math. Gen. **38**, 1419 (2005).

[45] O. Golinelli and K. Mallick, Spectral degeneracies in the totally asymmetric exclusion process, J. Stat. Phys. **120**, 779 (2005).

[46] C. Appert-Rolland, B. Derrida, V. Lecomte, and F. van Wijland, Universal cumulants of the current in diffusive systems on a ring, Phys. Rev. E **78**, 021122 (2008).

[47] S. Prolhac and K. Mallick, Current fluctuations in the exclusion process and Bethe ansatz, J. Phys. A: Math. Theor. **41**, 175002 (2008).

[48] S. Prolhac, Tree structures for the current fluctuations in the exclusion process, J. Phys. A: Math. Theor. **43**, 105002 (2010).

[49] K. Mallick, Some exact results for the exclusion process, J. Stat. Mech.: Theory Exp. (2011) P01024.

[50] D. Simon, Bethe ansatz for the weakly asymmetric simple exclusion process and phase transition in the current distribution, J. Stat. Phys. **142**, 931 (2011).

[51] K. Motegi, K. Sakai, and J. Sato, Exact relaxation dynamics in the totally asymmetric simple exclusion process, Phys. Rev. E **85**, 042105 (2012).

[52] I. Corwin, Two ways to solve ASEP, in *Topics in Percolative and Disordered Systems*, Springer Proceedings in Mathematics & Statistics (Springer, New York, 2014), pp. 1–13.

[53] S. Prolhac, Spectrum of the totally asymmetric simple exclusion process on a periodic lattice-first excited states, J. Phys. A: Math. Theor. **47**, 375001 (2014).

[54] S. Prolhac, Finite-time fluctuations for the totally asymmetric exclusion process, Phys. Rev. Lett. **116**, 090601 (2016).

[55] S. Prolhac, Extrapolation methods and Bethe ansatz for the asymmetric exclusion process, J. Phys. A: Math. Theor. **49**, 454002 (2016).

[56] S. Prolhac, Perturbative solution for the spectral gap of the weakly asymmetric exclusion process, J. Phys. A: Math. Theor. **50**, 315001 (2017).

[57] S. Prolhac, Riemann surface for TASEP with periodic boundaries, J. Phys. A: Math. Theor. **53**, 445003 (2020).

[58] Z. Liu, A. Saenz, and D. Wang, Integral formulas of ASEP and q-TAZRP on a ring, Commun. Math. Phys. **379**, 261 (2020).

[59] S. Prolhac, From the Riemann surface of TASEP to ASEP, J. Phys. A: Math. Theor. **54**, 395002 (2021).

[60] J. Baik and Z. Liu, Periodic TASEP with general initial conditions, Probab. Theory Relat. Fields **179**, 1047 (2021).

[61] J. D. Noh and D. Kim, Interacting domain walls and the five-vertex model, Phys. Rev. E **49**, 1943 (1994).

[62] G. M. Schütz, Exact solution of the master equation for the asymmetric exclusion process, J. Stat. Phys. **88**, 427 (1997).

[63] M. Alimohammadi, V. Karimipour, and M. Khorrami, Exact solution of a one-parameter family of asymmetric exclusion processes, Phys. Rev. E **57**, 6370 (1998).

[64] T. Sasamoto and M. Wadati, One-dimensional asymmetric diffusion model without exclusion, Phys. Rev. E **58**, 4181 (1998).

[65] B. Derrida and M. R. Evans, Bethe ansatz solution for a defect particle in the asymmetric exclusion process, J. Phys. A: Math. Gen. **32**, 4833 (1999).

[66] F. C. Alcaraz and R. Z. Bariev, Exact solution of the asymmetric exclusion model with particles of arbitrary size, Phys. Rev. E **60**, 79 (1999).

[67] V. Karimipour, A remark on integrability of stochastic systems solvable by matrix product ansatz, Europhys. Lett. **47**, 501 (1999).

[68] F. Roshani and M. Khorrami, Asymmetric one-dimensional exclusion processes: A two-parameter exactly solvable example, Phys. Rev. E **60**, 3393 (1999).

[69] F. Roshani and M. Khorrami, Solvable multispecies reaction-diffusion processes, Phys. Rev. E **64**, 011101 (2001).

[70] F. C. Alcaraz and R. Z. Bariev, Exact integrable spin chains and transfer matrices related to models with stochastic dynamics, Physica A **306**, 51 (2002).

[71] A. A. Ferreira and F. C. Alcaraz, Anomalous tag diffusion in the asymmetric exclusion model with particles of arbitrary sizes, Phys. Rev. E **65**, 052102 (2002).

[72] F. Roshani and M. Khorrami, Annihilation-diffusion processes: An exactly solvable model, J. Math. Phys. **43**, 2627 (2002).

[73] V. B. Priezzhev, Exact nonstationary probabilities in the asymmetric exclusion process on a ring, Phys. Rev. Lett. **91**, 050601 (2003).

[74] A. M. Povolotsky, V. B. Priezzhev, and C.-K. Hu, Finite size behavior of the asymmetric avalanche process, Physica A **321**, 280 (2003).

[75] A. M. Povolotsky, Bethe ansatz solution of zero-range process with nonuniform stationary state, Phys. Rev. E **69**, 061109 (2004).

[76] F. Roshani and M. Khorrami, A family of discrete-time exactly-solvable exclusion processes on a one-dimensional lattice, Eur. Phys. J. B **45**, 399 (2005).

[77] A. M. Povolotsky and J. F. F. Mendes, Bethe ansatz solution of discrete time stochastic processes with fully parallel update, J. Stat. Phys. **123**, 125 (2006).

[78] A. M. Povolotsky and V. B. Priezzhev, Determinant solution for the totally asymmetric exclusion process with parallel update, J. Stat. Mech.: Theory Exp. (2006) P07002.

[79] A. M. Povolotsky and V. B. Priezzhev, Determinant solution for the totally asymmetric exclusion process with parallel update: II. Ring geometry, J. Stat. Mech.: Theory Exp. (2007) P08018.

[80] S. N. Majumdar, K. Mallick, and S. Nechaev, Bethe ansatz in the Bernoulli matching model of random sequence alignment, Phys. Rev. E **77**, 011110 (2008).

[81] D. Simon, Construction of a coordinate Bethe ansatz for the asymmetric simple exclusion process with open boundaries, J. Stat. Mech.: Theory Exp. (2009) P07017.

[82] M. J. Lazo and A. A. Ferreira, Asymmetric exclusion model with impurities, Phys. Rev. E **81**, 050104 (2010).

[83] M. J. Lazo and A. A. Ferreira, Asymmetric exclusion model with several kinds of impurities, J. Stat. Mech.: Theory Exp. (2012) P05017.

[84] E. Lee, The current distribution of the multiparticle hopping asymmetric diffusion model, J. Stat. Phys. **149**, 50 (2012).

[85] A. Borodin, I. Corwin, L. Petrov, and T. Sasamoto, Spectral theory for interacting particle systems solvable by coordinate Bethe ansatz, Commun. Math. Phys. **339**, 1167 (2015).

[86] A. E. Derbyshev, A. M. Povolotsky, and V. B. Priezzhev, Emergence of jams in the generalized totally asymmetric simple exclusion process, Phys. Rev. E **91**, 022125 (2015).

[87] Z. Chen, J. de Gier, I. Hiki, T. Sasamoto, and M. Usui, Limiting current distribution for a two species asymmetric exclusion process, Commun. Math. Phys. **395**, 59 (2022).

[88] A. Saenz, C. A. Tracy, and H. Widom, Domain walls in the Heisenberg-Ising spin-1/2 chain, in *Toeplitz Operators and Random Matrices: In Memory of Harold Widom*, Operator Theory: Advances and Applications (Springer International Publishing, Cham, 2022), pp. 9–47.

[89] J. d. Gier, W. Mead, and M. Wheeler, Transition probability and total crossing events in the multi-species asymmetric exclusion process, J. Phys. A: Math. Theor. **56**, 255204 (2023).

[90] Y. Ishiguro, J. Sato, and K. Nishinari, Asymmetry-induced delocalization transition in the integrable non-Hermitian spin chain, Phys. Rev. Res. **5**, 033102 (2023).

[91] I. Lobaskin, M. R. Evans, and K. Mallick, Integrability of two-species partially asymmetric exclusion processes, J. Phys. A: Math. Theor. **56**, 165003 (2023).

[92] G. M. Schütz, The space-time structure of extreme current and activity events in the ASEP, in *Nonlinear Mathematical Physics and Natural Hazards* (Springer International Publishing, Cham, 2015), pp. 13–28.

[93] T. C. Dorlas, Orthogonality and completeness of the Bethe ansatz eigenstates of the nonlinear Schroedinger model, Commun. Math. Phys. **154**, 347 (1993).

[94] R. P. Langlands and Y. Saint-Aubin, Algebro-geometric aspects of the Bethe equations, in *Strings and Symmetries* (Springer, Berlin, 1995), Vol. 447, pp. 40–53.

[95] E. Brattain, N. Do, and A. Saenz, The completeness of the Bethe ansatz for the periodic ASEP, arXiv:1511.03762.

[96] D. R. Brillinger, The analyticity of the roots of a polynomial as functions of the coefficients, Math. Mag. **39**, 145 (1966).

[97] C. Timm, Random transition-rate matrices for the master equation, Phys. Rev. E **80**, 021140 (2009).

[98] S. Denisov, T. Laptyeva, W. Tarnowski, D. Chruściński, and K. Życzkowski, Universal spectra of random Lindblad operators, Phys. Rev. Lett. **123**, 140403 (2019).

[99] W. Tarnowski, I. Yusipov, T. Laptyeva, S. Denisov, D. Chruściński, and K. Życzkowski, Random generators of Markovian evolution: A quantum-classical transition by superdecoherence, Phys. Rev. E **104**, 034118 (2021).

[100] G. Nakerst, S. Denisov, and M. Haque, Random sparse generators of Markovian evolution and their spectral properties, Phys. Rev. E **108**, 014102 (2023).

[101] J. de Gier and F. H. L. Essler, Bethe ansatz solution of the asymmetric exclusion process with open boundaries, Phys. Rev. Lett. **95**, 240601 (2005).

[102] J. de Gier and F. H. L. Essler, Exact spectral gaps of the asymmetric exclusion process with open boundaries, J. Stat. Mech.: Theory Exp. (2006) P12011.

[103] J. de Gier, C. Finn, and M. Sorrell, The relaxation rate of the reverse-biased asymmetric exclusion process, J. Phys. A: Math. Theor. **44**, 405002 (2011).

[104] N. Crampe, E. Ragoucy, and D. Simon, Matrix coordinate Bethe ansatz: Applications to XXZ and ASEP models, J. Phys. A: Math. Theor. **44**, 405003 (2011).

[105] V. Alba, Eigenstate thermalization hypothesis and integrability in quantum spin chains, Phys. Rev. B **91**, 155123 (2015).

[106] B. Gaveau, L. S. Schulman, and L. J. Schulman, Imaging geometry through dynamics: The observable representation, J. Phys. A: Math. Gen. **39**, 10307 (2006).